Available online at www.sciencedirect.com

ScienceDirect

Advances in Space Research 73 (2024) 64–84

ADVANCES IN SPACE RESEARCH
(a COSPAR publication)

www.elsevier.com/locate/asr

RSO proper elements: Concept, methods, and application to maneuver detection

Di Wu [a,b,*], Lamberto Dell'Elce [c], Aaron J. Rosengren [a]

[a] Department of Mechanical and Aerospace Engineering, UC San Diego, La Jolla, CA 92093, USA
[b] Department of Aeronautics and Astronautics, Massachusetts Institute of Technology, Cambridge, MA 02139, USA
[c] Université Côté Azur and Inria Sophia Antipolis Méditerranée, 06902 Valbonne, France

Received 7 February 2023; received in revised form 6 August 2023; accepted 22 August 2023
Available online 25 August 2023

Abstract

Asteroid families consist of swarms of fragments generated after energetic interasteroidal collisions in the distant past that resulted in the breakup of their progenitors. They are recognized by searching for clusters in the three-dimensional space of "proper elements"; parameters characterizing the asteroid orbits that are very close to fundamental invariants of motion, and thus keep a dynamical record of the initial proximity of the orbits generated by a catastrophic fragmentation event. In the circumterrestrial context, proper elements have recently been applied to the dynamical taxonomy of resident space objects (RSO) for the association of debris from breakup into its "parent" satellite. Here, we clarify, adapt, and extend this fundamental concept to space situational awareness for on-orbit maneuver/anomaly detection. RSO proper elements, being linked to the underlying dynamical structure of orbits, can provide a more robust metric within existing maneuver-detection algorithms, through assessment of the induced changes in these quasi invariants of the motion. We highlight the deeper connection of proper elements to classical frozen orbits in Earth-satellite dynamics and to secular elements in artificial satellite theories based on canonical perturbation theory and showcase several techniques for their numerical computation, including a newly proposed Ptolemy method; applicable to both the asteroid and space-debris domains. We apply a Bayesian online changepoint-detection (BOCD) algorithm in both mean- and proper-element space and compare their performances for orbit-maneuver detection.

Keywords: Astrodynamics; Orbital maneuvers; Space debris; Space situational awareness

1. Introduction

As near-Earth space gets more and more congested, contested, and competitive, a rigorous classification scheme based upon scientific taxonomy is needed to properly identify, group, and discriminate resident space objects (RSOs) (Jankovic and Kirchner, 2018; Mellish and Frueh, 2021). Any attempt to classify debris, say, into "families" cannot be based on the osculating elements, which, being in continual change as functions of time, do not clearly disclose any characteristic features of the initial orbit or state vector. Mean orbital elements, such as those provided by the two-line element sets (TLEs) of the space-object catalog (SOC) (Chao and Hoots, 2018; Vallado, 2022), also do not leave a dynamical fingerprint of the object's inherent state, since they vary over longer (secular) timescales. Proper orbital elements, however, are obtained as a result of the elimination of short- and long-periodic perturbations from their instantaneous, osculating counterparts,

* Corresponding author at: Department of Mechanical and Aerospace Engineering, UC San Diego, La Jolla, CA 92093, USA.
E-mail addresses: d8wu@ucsd.edu, d_wu@mit.edu (D. Wu), lamberto.dell-elce@inria.fr (L. Dell'Elce), ajrosengren@eng.ucsd.edu (A.J. Rosengren).

https://doi.org/10.1016/j.asr.2023.08.038
0273-1177/

and therefore represent a true kind of average characteristic of motion (Knežević et al., 2002). Recently, using detailed Hamiltonian-perturbation theory, Celletti et al. (2021, 2022) has shown the utility of proper elements for the association of space debris from a fragmentation event into its "parent" satellite, akin to what has been done over the past hundred years by small-body taxonomists in characterizing asteroid families (Hirayama, 1918; Brouwer, 1951; Murray and Dermott, 1999; Nesvorný et al., 2015; Novaković et al., 2022; Zappalà et al., 1990; Milani et al., 2014).

The fundamental notion of asteroid proper elements arose from the classical Laplace-Lagrange "secular" solution describing the gravitational interactions of Jupiter and Saturn on small-body orbits (Murray and Dermott, 1999; Knežević et al., 2002). The disturbing function, when expanded as an infinite series, gives rise to the separation of perturbing effects into periodic and secular variations and the distinction between fast and slow time variables. The proper elements are the secular elements for the corresponding dynamical model and order of the perturbation theory that built them. The approximation of the linear secular perturbation theory is sufficient for a time span of the order of the period of circulation of the longitude of pericenter. While improvements can be made using elaborate higher-order analytical theories based on lie-series canonical transformations, presently, the method of choice to compute more "accurate", in the sense of stable, unchanging, proper elements is to integrate the equations of celestial dynamics, and extract constants of motion directly from a numerical analysis of the predicted positions (Knežević et al., 2002; Nesvorný et al., 2015).

Although modern formulations obtain the (synthetic) proper elements by numerically integrating the orbits over millions of years and applying Fourier analysis (Knežević et al., 2002), the device of canonical transformations, ubiquitously employed in both asteroid and artificial-satellite dynamics, permits a deeper understanding of the difference between osculating, mean (orbit-averaged), and secular (or proper) elements (Morbidelli, 2002; Lara, 2021). Classically, approximate analytical solutions of the Lagrange equations were sought in terms of developments in trigonometric series with respect to the small parameters of the problem (the dominant oblateness gravity-field coefficient, J_2, for instance, in the satellite problem); successive powers of these parameters figured as factors in the coefficients of the series, the arguments being functions of time. The procedure of integration brought to light a very remarkable class of perturbations; that is, the appearance of perturbations of seemingly secular character. These perturbations result from terms that contain the time variable explicitly, and not only in the arguments of sine and cosine, and seem to indicate that the solution increases without bound in the course of time. The fact that the general solution involves power series in the time suggests, however, that these secular terms are merely the first terms in the series representation and may actually be equivalent to terms of very long period. Astronomers have, nevertheless, traditionally adopted the use of secular, rather than mean, to describe the long-term, orbit-averaged evolution.

Brouwer (1959), using the von Zeipel perturbation method to treat the drag-free motion of a satellite about an oblate planet, obtained an intricate analytical solution to the zonal-harmonics problem through a succession of canonical transformations that rendered the transformed Hamiltonian a function of only the conjugate canonical momenta. These double-primed variables in Brouwer's notation, known in astrodynamical parlance as secular elements, are constants under Brouwer's theory and would thus be termed the satellite's proper elements under the adopted zonal-harmonics model. Nevertheless, the distinction between secular and mean has often been muddled in the literature (Cain, 1962; Breakwell and Vagners, 1970) with tabulated mean-to-osculating transformations (Alfriend et al., 2009; Schaub and Junkins, 2018) inaptly applying Brouwer's full periodic corrections. Under a general harmonic analysis of the perturbations, the osculating elements undergo secular, long-period, and short-period variations, with the mean (orbit-averaged) elements capturing both the secular drift and long-periodic oscillations. True secular behavior in the action variables, however, in which the semi-major axis, eccentricity, or inclination changes in a linear fashion, cannot occur in Earth-satellite dynamics as a result of dissipative forces (e.g., atmospheric drag) or chaotic diffusion brought about by various orbital resonances (Rosengren et al., 2019b). All of these subtleties and nuances, including the effects of additional gravitational and non-gravitational perturbations, may be relevant and must be considered for the circumterrestrial context.

Satellite-maneuver detection is concerned with finding anomalies in an evolution. Li et al. (2018) and Lemmens and Krag (2014b) treat maneuver/anomaly detection as a statistics problem by proposing different moving-window-segmentation and threshold-calculation methods, both based on historical TLE data. These works extend earlier analysis of Kelecy et al. (2007), who used a similar data-filtering and threshold-checking strategy. Later developments, employing more complex dynamics, focus on integrating maneuver detection in space surveillance and tracking; namely, using tracking data directly. Pirovano and Armellin (2022) employ a convex-optimization formulation that defines a threshold with the Mahalanobis distance and uses state deviation, calculated by the conjugated-unscented transform (CUT), to not only detect but also estimate maneuvers under an optimalilty assumption. Research with variations in the detailed techniques describing the motion of a satellite accomplishing a maneuver, such as thrust-Fourier coefficients (Ko and Scheeres, 2015) or multi-hypothesis tracking (Zucchelli et al., 2020), shows promise. Similarly, the integration of Monte-Carlo-sampling schemes, multi-fidelity dynamics, and multi-hypothesis maneuver detection has been used in track-to-orbit association in Porcelli et al. (2022); and in maneuver inference following Bayesian processes in Escribano et al. (2022). While combining tracking and maneuver detection would be beneficial for associating objects and maintaining catalogues (Pastor et al., 2022), the dynamics employed is generally straight-forward osculating or mean dynamics without taking advantage of the inherent information masked by the evolution.

Here, we investigate and extend the fundamental concept of proper elements for use in on-orbit maneuver/anomaly detection of satellites in low-Earth orbit (LEO). We first review the concept of asteroid proper elements and the various analytical, semi-analytical, and synthetic (numerical) theories adopted for their computation (Section 2). We then propose a new generalized approach — the Ptolemy method — applicable to both asteroid and RSO dynamics and compare it to the state-of-the-art for the determination of proper elements of cataloged asteroids. We recount several pertinent analytical theories of motion of Earth-satellite orbits, which can be used to compute RSO proper elements, and compare their accuracy to the Ptolemaic numerical scheme across increasingly complex dynamical models (Section 3 & Appendix A). Proper elements, due to their quasi constancy in time under natural perturbations, provide a sui generis and hitherto unexplored orbital signature for assessing unmodeled maneuvers or mismodeled dynamics. We apply a Bayesian online changepoint-detection (BOCD) algorithm in both mean- and proper-element space and compare their performances for maneuver detection under multiple scenarios of thrust magnitudes and directions.

2. Asteroid proper elements

According to the classical Laplace-Lagrange secular (i.e., orbit-averaged) solution (Murray and Dermott, 1999), the mean eccentricity e of the asteroid in the $(k,h) = (e\cos\varpi, e\sin\varpi)$ plane is given by the vector sum of the forced and free (proper) components, as shown in Fig. 1. The asteroid's mean eccentricity can be thought of as motion around a circle with center (k_0, h_0) at a constant rate; the center of the circle that the free (proper) eccentricity precess around is the forced eccentricity. The forced eccentricity e_f and forced longitude of pericenter ϖ_f are determined solely by the semi-major axis of the particle and the secular solution for the perturbing bodies. The free eccentricity e_p and free longitude of pericenter ϖ_p, on the other hand, are derived from the initial conditions and denote fundamental orbital parameters of the asteroid; hence, why these quantities are also referred to as the proper elements. In the linear secular theory, eccentricity and inclination are decoupled, and an analogous situation holds for the inclination when projected in the $(q,p) = (i\cos\Omega, i\sin\Omega)$ plane. Note that by limiting the disturbing function to its secular and long-periodic parts, the mean semi-major axis becomes a constant of the motion and, consequently, the first proper element a_p.

2.1. Ptolemy method

In discussing the connection between "proper modes", whose amplitudes are noted to be proper elements in Knežević and Milani (2000), and the linear theory of secular perturbations, under the section *Proper Elements/Parameters* in Knežević et al. (2002), Knežević et al. mention the connection between the orbital evolution of asteroids in the (k,h) and (q,p) planes and epicyclic motion. Murray and Dermott (1999) give the detailed derivation for the expressions of forced elements and free elements (an analogous term for proper elements), and those imply that an asteroids motion could indeed be thought of as "motion around a circle at a constant rate" with the "center moving at a complicated path". The (k,h) and (q,p) planes have their own "proper circle" and the radii of these correspond to proper eccentricity e_p and proper inclination i_p, respectively.

The Ptolemy method for proper eccentricity e_p and proper inclination i_p capitalizes on the geometrical interpretations of proper elements and can be summarized by the following steps, akin to the synthetic method proposed in Knežević and Milani (2000):

1. Propagate the initial condition to get a full sequence of orbital elements and project those orbital elements into (h,k) and (q,p), respectively;
2. Divide the whole sequence into N segments in (h,k) or (q,p);
3. Go over all segments and find the best circle fit; record the corresponding radius for each segment's proper elements;
4. Calculate the mean and RMSE of all segments' proper elements as this sequence's proper elements, either proper eccentricity e_p or sine of proper inclination sin i_p, and the corresponding RMSE.

In short, the Ptolemy-method algorithm, summarized as Alg. 1, applies the geometrical relationship between proper elements and the projected evolution in (k, h) and (q, p) planes to find these parameters uniquely determined by the object and the dynamics. While the Ptolemy method focuses on extracting proper elements from both (k, h) and (q, p) planes, the proper semimajor axis a_p could also be calculated by replacing the circle fitting part with a simple averaging procedure with the short-periodic perturbation excluded from the dynamics.

We summarize the algorithm in this general way to enable its adaptability in different situations. The propagation step is left out of the core part of the algorithm as the propagation sequence could go through different processing. In the asteroids case, similar to the steps in the synthetic method (Knežević et al., 2002), the propagated osculating elements would go through a low-pass filter, with design parameters specified in Knežević et al. (2002) to filter out short-periodic evolution. In addition, the step of removing fundamental frequencies (Knežević et al., 2002) of Jupiter, Saturn, Uranus, and Neptune from (h, k) and of Saturn, Uranus, Neptune from (q, p) is also applied in the asteroids case in our comparison study, in Section 2.2, between the synthetic method and the Ptolemy method.

The general Ptolemy algorithm expression could adopt to different phase plane under the support of a theory that validates the phase plane. In asteroids case, the phase plane is $(k, h) = (e\cos\varpi, e\sin\varpi)$, where $\varpi = \Omega + \omega$ is supported by the theory of Laplace-Lagrange secular theory in Murray and Dermott (1999). While Murray and Dermott (1999) adopt $(q, p) = (i\cos\Omega, i\sin\Omega)$, resulting in proper inclination i_p, sine of inclination or even tangent of inclination are sometimes used in different computation methods. The synthetic method uses the expression of the sine of inclination, so we adopt the (q, p) plane expression accordingly as $(q, p) = (\sin i\cos\Omega, \sin i\sin\Omega)$. In the RSO case, the phase planes are $(k, h) = (e\cos\omega, e\sin\omega)$ and $(q, p) = (\sin i\cos\omega, \sin i\sin\omega)$, naturally arising from the classical theories of frozen satellite orbits.

Algorithm 1. The Ptolemy method

Algorithm 1: The Ptolemy method

Result: Find proper element and RMSE for a propagation sequence separated by a prescribed segmentation
Input : Propagation sequence S and the number of segments N
Output: Proper element p and RMSE σ

/* separate the sequence S into N segments $s_1, s_2, \dots, s_N$ */
$s_1, s_2, \dots, s_N \leftarrow \text{sequence\_segmentation}(S, N)$
/* calculate proper elements for segments $s_1, s_2, \dots, s_N$ */
for $i = 1, 2, \dots, N$ **do**
  /* extract either (k, h) or (q, p) components from a segment s_i */
  $(k, h) \leftarrow s_i$ or $(q, p) \leftarrow s_i$
  /* fit a circle over (k, h) or (q, p) and */
  /* extract circle's radius r_i */
  $r_i \leftarrow \text{circle\_fit}(k, h)$ or $\text{circle\_fit}(q, p)$
  /* record the segment's proper element */
  $p_i \leftarrow r_i$
end
/* average over all segments proper elements to find mean and RMSE */
/* record whole sequence's proper element p and RMSE σ */

$$p \leftarrow \frac{1}{N}\sum_{i=1}^{N} p_i,\ \sigma \leftarrow \sqrt{\sum_{i=1}^{N}\frac{(p_i - p)^2}{n}}$$

return p, σ

The application of the circle-fitting procedure in Alg. 1, exploring the geometrical interpretation, could be achieved in different ways. From the detailed explanation and comparison discussed in Gander et al. (1994) and Al-Sharadqah and Chernov (2009), we use the popular Pratt fit — an algebraic, rather than a geometrical, fit that balances between computational requirements and accuracy — as the circle-fitting algorithm. In short, instead of minimizing the orthogonal distance in the geometrical fit, Pratt fit minimizes a modified polynomial function that results in an increase in speed and decrease in computation. In our experiment, Pratt fit's pitfall of converging towards a smaller radius in short arcs is conveniently avoided by providing near circular or overlapping arcs. However, we do find through our studies that the Kasa and Taubin fits (Al-Sharadqah and Chernov, 2009) tend to either require longer computation or yield absurd results. The geometrical fit performs at the same level as the Pratt fit at an expense of computational power; hence why we adopted the latter method for the circle-fitting procedure.

In addition, the segmentation applied over the sequence is done in an equal-size, minimum-overlapping way. For a sequence of length L and N segments target, we find the residual of L dividing $N: R = rem(L/N)$. Then we find the stepping size between each segment's starting index to be $s = (L - R)/N$ and the length of each segment to be $l = s + R$. So for each segment, the starting indexes are $1, s + 1, 2s + 1, \dots, Ns + 1$ and the ending indexes are $l, s + l, 2s + l, \dots, Ns + l$.

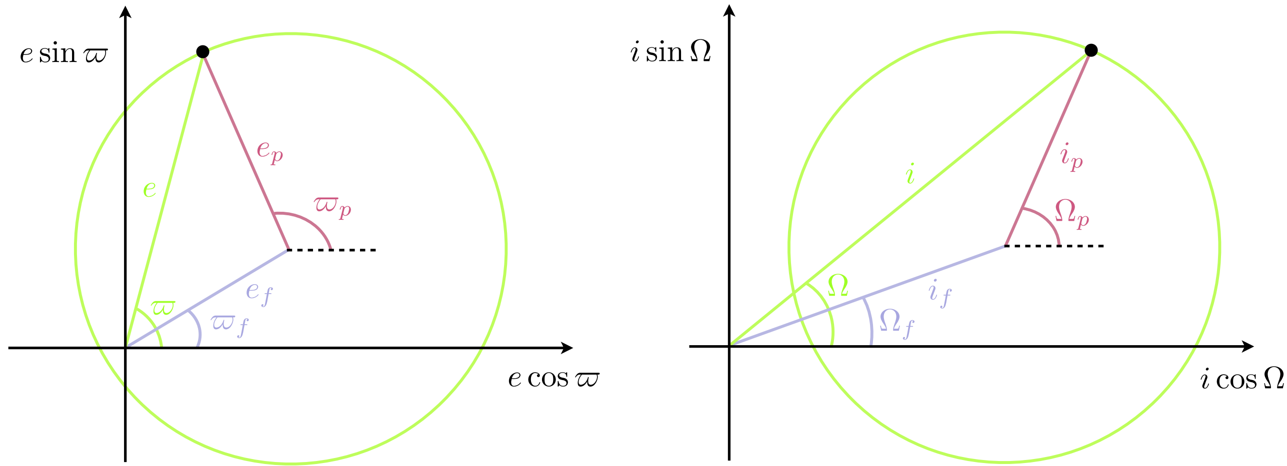

Fig. 1. The geometrical relationship among the mean, free, and forced elements, adapted from Murray and Dermott (1999). The mean eccentricity e of the orbit (*left*) can be resolved vectorially into two components: a forced eccentricity e_f, imposed by the perturbations in the system; and a free (proper) eccentricity e_p, that is determined by the initial conditions. The corresponding mean, forced, and proper longitudes of pericenter ϖ, ϖ_f, and ϖ_p define the orientation of the orbit with respect to an arbitrary fixed direction. Shown here is the case $e_p > e_f$, but it is important to note that the circle need not encompass the origin. In the $(q, p) = (i \cos \Omega, i \sin \Omega)$ plane (*right*), i_f, Ω_f, i_p, and Ω_p denote the forced and free inclinations and longitudes of ascending node, respectively. Illustrated here is a situation where $i_p < i_f$, such that the circle does not enclose the origin.

Furthermore, since the RMSE from the Ptolemy method is related with the segmentation and length of propagation while being an indicator for the quality of the proper elements, this Ptolemy method could be improved by incorporating multiple optimization methods to explore the optimal parameters for improving the proper elements' quality.

2.2. Results in the asteroids case

Although the true curves described by the asteroid's mean eccentricity and inclination are not strictly circles, or for that matter, any regular formed curve, this simplified geometrical picture forms the template about which their motion is understood and described (Knežević et al., 2002). Under the approximations of the Laplace-Lagrange theory, the proper elements correspond to the constants of integration of the solutions of the averaged equations of motion. In the Hamiltonian-perturbation formalism, these quasi-integrals of motion can be obtained as a result of the elimination of the short-periodic perturbations (terms that depend on the fast-varying mean anomaly) and long-periodic perturbations (harmonics dependent on the perihelia and nodes) (Morbidelli, 2002). The accuracy, long-term stability, and reliability of the computed proper elements is limited by the order truncation (in the small parameter) of the perturbation theory and by the degree truncation (in the eccentricities and inclinations). The synthetic (numerical) method is based on the post-processing of a numerical integration of the asteroid's orbit under a realistic dynamical model over secular timescales (Knežević et al., 2002). The short-periodic perturbations are removed through numerical averaging and the resulting time series is spectrally resolved using Fourier analysis to remove the main forced terms and extract principal harmonics (proper values). The computed proper elements are tested for accuracy and stability by performing running box tests to measure the deviation of these elements from constancy. The tests consist of producing a time series of proper elements, using the procedure outlined, over shorter time intervals distributed over the entire span covered by the integrations, thus providing a set of distinct values of elements for each time window to be used to compute error estimates (e.g., standard deviations and maximum excursions).

Being computed by means of different procedures (analytical, semi-analytical, numerical) and sometimes even defined in different ways (e.g., for resonant asteroids), reported proper elements are of different accuracy and long-term reliability. The synthetic method currently produces the most stable values and the Asteroids Dynamic Site, `AstDyS-2`, database lists these proper elements for hundreds of thousands of cataloged asteroids. Because the orbits of circumterrestrial satellites and space debris, and their dynamical environments, differ so markedly from the classical problems presented by nature, many of the time-honored methods of Solar-System celestial mechanics are inapplicable. While the Hamiltonian formalism has shown success in the high-altitude regimes (Celletti et al., 2021; Celletti et al., 2022), in which the dynamics is largely governed by conservative forces, the dissipative and Earth-gravity-field dominated region of LEO presents additional challenges. The Fourier-based synthetic method, in principle, can be adopted for the satellite problem, but the forced frequency modes are not as sufficiently well separated or of distinct amplitudes to permit satisfactory modeling. Although other frequency-spectrum techniques may be applied, we have instead devised a new synthetic method that capitalizes on the epicyclic nature of the perturbed Kepler problem, connecting the classical Laplace-Lagrange theory with its analog in Earth-satellite dynamics — namely, frozen orbits. With the moniker, the Ptolemy method, or the Ptolemy-epicyclic method for completion, the proposed numerical scheme follows a similar procedure as the standard synthetic method, outlined above. But rather than analyzing the post-processed, mean-element space in the frequency domain, this approach optimally fits discrete running-box segments of the filtered osculating trajectory to obtain characteristic epicyclic circles and averages their radii to produce statistically relevant proper elements for the trustworthy detection of on-orbit maneuvers. While somewhat heuristic by nature, we first validate the Ptolemy method computation against several cataloged asteroids with known stable proper elements. The specific procedure is outlined in Section 2.1 and described in more detail in Wu and Rosengren (2019) and Wu (2022), to which we refer for more details. Fig. 2 provides an illustrative example of the approach applied for both a simplified dynamical model (Laplace-Lagrange theory) and realistic N-body simulation, obtained using the `IAS15` integrator within `REBOUND` (Rein and Spiegel, 2015). The projected motion in both cases is a combination of uniform rotation in a circle, where the center of the circle is executing some prescribed path in (k, h), dependent only on the secular evolution of the perturbing bodies.

The results for asteroid, 221 Eos, is shown in Table 1a, a, together with that reported by Murray and Dermott (1999), based on the analytical Laplace-Lagrange theory, as well as the `AstDyS-2` database synthetic and analytical results. We also considered asteroids Sylvia(87), 69 Hesperia, and 25045 Baixuefei. The orbit of Eos was propagated using `REBOUND`, adopting a dynamical model that contains the seven major planets (from Venus to Neptune) as perturbers. The propagation, required for both synthetic method and Ptolemy method, is conducted according to the data provided in `AstDyS-2`: 221 Eos, Sylvia(87), and 69 Hesperia are backwards propagated 2 million years, while 25045 Baixuefei is forward propagated over 2 million years; all the propagation are conducted with a 5-year step size. For completeness and validation, we applied the Fourier-based synthetic method on the outputted trajectory and computed the variance/root-mean-square error (RMSE). As reported by `AstDyS-2`'s synthetic method paper (Knežević and Milani, 2000), the segment number N is 11 for any 2-million-year-propagation case. We adopt the same segment number in the comparison shown in Table 1.

Proper elements are dynamics-specific. Thus, the consistency in dynamics is important in comparing proper-elements accuracy. The `AstDyS-2` synthetic proper elements are created in "a model including the full perturbations by the four giant planets, and with a correction to account for most of the indirect effect of the inner planets" (Milani and Knežević, 1994) using the `ORBIT9` propagator. They appear to be different from the synthetic proper elements recreated following the same synthetic method (Knežević and Milani, 2000) in a 7-planet dynamics model using `REBOUND`. In addition, different parameters used in the propagation, such as the removed forced frequency, the method used in frequency removal itself, and the approach used in filtering the osculating states in the pre-processing stage, could all result in discrepancies. A more insightful comparison between the synthetic method and Ptolemy method can therefore be achieved when both are evaluated under the same dynamics model, ensuring a fair assessment.

Comparing between the proper elements from the recreated synthetic method and the Ptolemy method, Ptolemy

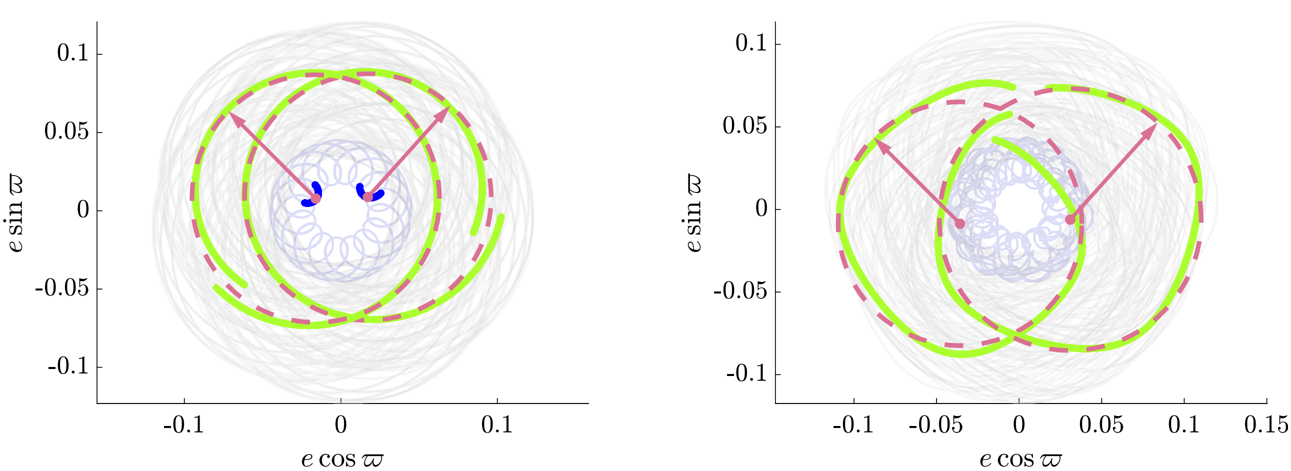

Fig. 2. Illustration of the Ptolemy method for proper-elements computation. The orbit of asteroid, 221 Eos, over 2 Myr projected in the (k, h) plane (*gray*), propagated using the Laplace-Lagrange theory (Murray and Dermott, 1999) (*left*) and the N-body integrator `REBOUND` (Rein and Spiegel, 2015) (*right*), considering perturbations from Jupiter and Saturn. The osculating trajectory from `REBOUND` has been digitally smoothed to remove short-periodic perturbations. The forced eccentricity, shown in *purple*, varies along an epicyclic path determined only by the secular evolution of the perturbing bodies. The *green* curves mark the segments of the trajectory used in the Ptolemy method to optimally-fitted epicycles (*pink*), from which the statistical proper eccentricity can be obtained. The corresponding forced-eccentricity evolution segments are marked in *blue*.

Table 1
Comparison of proper element values for main-belt asteroids, Eos (221), Sylvia (87), Hesperia (69), and Baixuefei (25045) at modified Julian date (MJD) 58400, obtained from different methods: Murray and Dermott (1999) (M&D) analytic, `AstDyS-2` analytic and synthetic, synthetic method reproduction, and the Ptolemy method.

(a) 221 Eos proper elements and corresponding RMSE values.

	e_p	e_p RMSE	$\sin i_p$	$\sin i_p$ RMSE
M&D Analytic	7.1000E-02	NaN†	1.7700E-01††	NaN†
`AstDyS-2` Analytic	7.69E-02	NaN†	1.726E-01	NaN†
`AstDyS-2` Synthetic	7.2611E-02	1.0900E-03	1.7123E-01	4.6900E-04
Synthetic Method	7.5478E-02	0.7492E-03	1.7231E-01	4.9054E-04
Ptolemy Method	8.0337E-02	0.7792E-03	1.7159E-01	4.1975E-04

(b) Sylvia(87) proper elements and corresponding RMSE values.

	e_p	e_p RMSE	$\sin i_p$	$\sin i_p$ RMSE
`AstDyS-2` Analytic	5.4E-02	NaN†	1.695E-01	NaN†
`AstDyS-2` Synthetic	5.3677E-02	1.0990E-04	1.7104E-01	3.3000E-05
Synthetic Method	5.9886E-02	3.2186E-04	1.7192E-01	29.1196E-05
Ptolemy method	6.7224E-02	3.5869E-04	1.7104E-01	10.3234E-05

(c) 69 Hesperia proper elements and corresponding RMSE values.

	e_p	e_p RMSE	$\sin i_p$	$\sin i_p$ RMSE
`AstDyS-2` Analytic	1.78E-01	NaN†	1.537E-01	NaN†
`AstDyS-2` Synthetic	1.7965E-01	9.8930E-04	1.5497E-01	1.7400E-05
Synthetic Method	1.8278E-01	14.5368E-04	1.5611E-01	22.5917E-05
Ptolemy method	1.8537E-01	15.5445E-04	1.4489E-01	12.14855E-05

(d) 25045 Baixuefei proper elements and corresponding RMSE values.

	e_p	e_p RMSE	$\sin i_p$	$\sin i_p$ RMSE
`AstDyS-2` Analytic	1.431E-01	NaN†	1.094E-01	NaN†
`AstDyS-2` Synthetic	1.4327E-01	1.1086E-03	1.1214E-01	7.1350E-04
Synthetic Method	1.3825E-01	1.0051E-03	1.1646E-01	25.5297E-04
Ptolemy method	1.4689E-01	1.1118E-03	1.1664E-01	21.8339E-04

† M&D and `AstDys` Analytic data do not report RMSE values.
†† M&D provides proper inclination 10.2°.

method yields a similar-level (5 out of the 8 cases) or better (3 out of the 8 cases) internal accuracy. It can be seen for the case of Eos that the Ptolemy method provides similar accuracy in proper eccentricity e_p and sine of proper inclination $\sin i_p$ as the recreated synthetic method. We also consider three additional main-belt asteroids, 87 Sylvia in Table 1b, in Hesperia Table 1c, and 25045 Baixuefei in Table 1d, for additional validation. The accuracy for the three asteroids' sine of proper inclination $\sin i_p$ from the Ptolemy method is superior to their counterparts from the synthetic method. However, when it comes to proper eccentricity e_p, both methods exhibit similar levels of accuracy.

Beside being dynamics-specific, proper elements are method-specific as well. Under the same dynamics model propagated in the same way under `REBOUND`, the Ptolemy method produces a different proper eccentricity, at a magnitude around 6×10^{-3}, compared to the synthetic method. The observed differences can be attributed to the discrepancy between the synthetic method's Fourier analysis, which employs a mode-analysis interpretation for proper elements, and the Ptolemy method's circle fitting, which adopts a geometrical interpretation for proper elements. The universal connection among those heuristically different methods is the quasi-constant feature of proper elements. Yet, a general and standardized way of quantifying different methods in calculating proper elements could be a potential extension to the existing works.

3. RSO proper elements

The notion of proper elements is not completely foreign to the geocentric domain; it has only been masked by the needs of astrodynamical practice and a specialized nomenclature. The fixed or forced eccentricity is, in fact, analogous to the familiar concept of frozen orbits in artificial-satellite theory (Cook, 1966; Coffey et al., 1994). The classical Laplace-plane equilibrium, characteristic of both natural and artificial satellites systems (Allan and Cook, 1964; Tremaine et al., 2009; Rosengren et al., 2014; Gachet et al., 2017), represents the fixed or forced inclination under an approximate dynamical model of oblateness and third-body perturbations. As previously noted in Section 1, the secular elements correspond to the proper elements for Brouwer's theory of satellite motion under oblateness perturbations (Brouwer, 1959) and equivalently for Giacaglia's theory for lunisolar perturbations (Giacaglia, 1974). More recently, the concept of proper elements has been investigated in the geosynchronous region by Gachet and colleagues (Gachet et al., 2017), extended to other circumterrestrial domains by Celletti et al. (Celletti et al., 2021; Celletti et al., 2022), and applied for lunar orbiters by Knežević and Milani (Knežević and Milani, 1998), each using detailed Hamiltonian-perturbation theory.

In Appendix A, we recount some of these analytical theories of proper elements in the satellite problem and compare their solutions to those obtained from the Ptolemy and synthetic methods, considering a hierarchy of more realistic, and more complicated, dynamical models. An essential aspect of the Fourier-based synthetic method is the removal of the forced frequency; yet, in the geocentric case, specifying the frequency associated with the forced term is more challenging, let alone the intrinsic spectral leakage resulting from the various gravitational and non-gravitational perturbations acting in concert. For these reasons, the Ptolemy method provides the most accurate and stable RSO proper elements, required for detecting orbit maneuvers.

3.1. RSO osculating, mean, and proper elements

A set of osculating elements has a correspondingly one-to-one set of instantaneous Cartesian states, given by the position and velocity vectors. Mean elements are defined as the averaging of osculating elements over one revolution of the mean anomaly M. Consequently, the dynamics of the "mean" mean anomaly reduce to quadratures and the averaged equations are no longer explicit functions of time. Moreover, from the Lagrange planetary equation governing the evolution of semi-major axis (a), averaging over mean anomaly in the perturbation function would render the semi-major axis constant throughout the evolution. Thus, the mean semi-major axis is constant theoretically. But, as the averaged perturbation function may still depend on the mean argument of perigee (ω) and right ascension of the ascending node (Ω), the mean eccentricity (e) and mean inclination (i), accordingly, could still oscillate over long secular periods; particularly, if the timescale is comparable to the evolutions of ω and Ω.

A comparison for the evolution of osculating, mean, and proper elements is illustrated in Fig. 3, under two different timescales of 0.1 and 100 days. A model composing of 10×10 Earth harmonics, lunisolar, SRP, and drag perturbation is used. In the 100-day evolution scenario, the long-term oscillation of both mean eccentricity and mean inclination due to the perturbation is obvious. The magnitude of those oscillations are not small enough to be neglected especially compared to the evolution of proper eccentricity and proper inclination. Contrasting with mean and osculating eccentricity and inclination, proper eccentricity and proper inclination have been shown to be "quasi-constant" throughout the evolution. In the long-term evolution, as discussed above, the mean semi-major axis is constant. The proper semi-major axis follows the same evolution as the mean semi-major axis. After zooming into the short-term evolution window of 0.1 days, we get another perspective of the evolution. In the 0.1-day time span, since the evolution window is so short compared to the mean eccentricity and inclination's oscillation periods, it appears that the mean eccentricity and inclination are "artificially" constant as there is not sufficient time for their changes to be visible. There are obvious offsets between proper elements evolution and mean elements evolution. These gaps come from the difference between the real long-term "quasi-constant" proper-elements values and the "artifically" windowed temporary constant mean-elements values. Throughout the two different time scales, the osculating elements are oscillating around the mean elements as one can infer from the averaging definition.

3.2. Proper elements at the corresponding model truncation

Theoretically, the proper elements retrieved from a true model would yield the most quasi-constant elements. However, in practice, one can only approximate the true dynamics using a truncated model. We show here the sensitivity of the proper elements to model truncation, by converting a time series of osculating elements, obtained from a "truth model," to different time series of proper elements under various model truncation.

The 100-day osculating-elements time series, shown in Fig. 3, was generated from a "full" model of 10×10 Earth-gravity harmonics, lunisolar, SRP, and drag perturbations. This model is considered the "truth" model in this analysis. Four different models of various truncation are used to obtain their corresponding proper elements in Fig. 4: the 10×10 full model of third-body and non-grav. perturbations; a reduced 8×8 Earth-harmonics model; a further simplified 5×5 truncation; and a 5×5 that does not include the additional third-body or non-grav. forces.

The proper elements from the 10×10 full model exhibit the least oscillation. While still containing lunisolar, SRP, and drag perturbation, as the degree and order of the Earth-harmonics model decreases, the 8×8 full model or the 5×5 full model would yield proper elements with correspondingly larger oscillation. Moreover, the proper elements from the higher accuracy model oscillate less than the ones from the lower accuracy model since the times series from the 5×5 full model have a much larger oscillation then those from the 8×8 full model. Stripping off lunisolar, SRP, drag perturbation, as well as additional tesseral and sectorial Earth harmonics, not only do the time series from the 5×5 zonal-harmonics-only model generate larger oscillation but these time series also create visually clear offsets in semi-major axis, eccentricity, and inclination.

It is worth noting the numerical process of converting osculating elements into proper elements depends on the corresponding truncated model (see, e.g., Appendix A). A consistent model for both osculating-orbital-elements generation and proper-elements transformation would result in the best "quasi-constant" proper elements. As the discrepancy between the osculating elements model and the model used for proper elements conversion grows, oscillations in proper elements start to appear. In addition, despite the small contribution drag could have on this

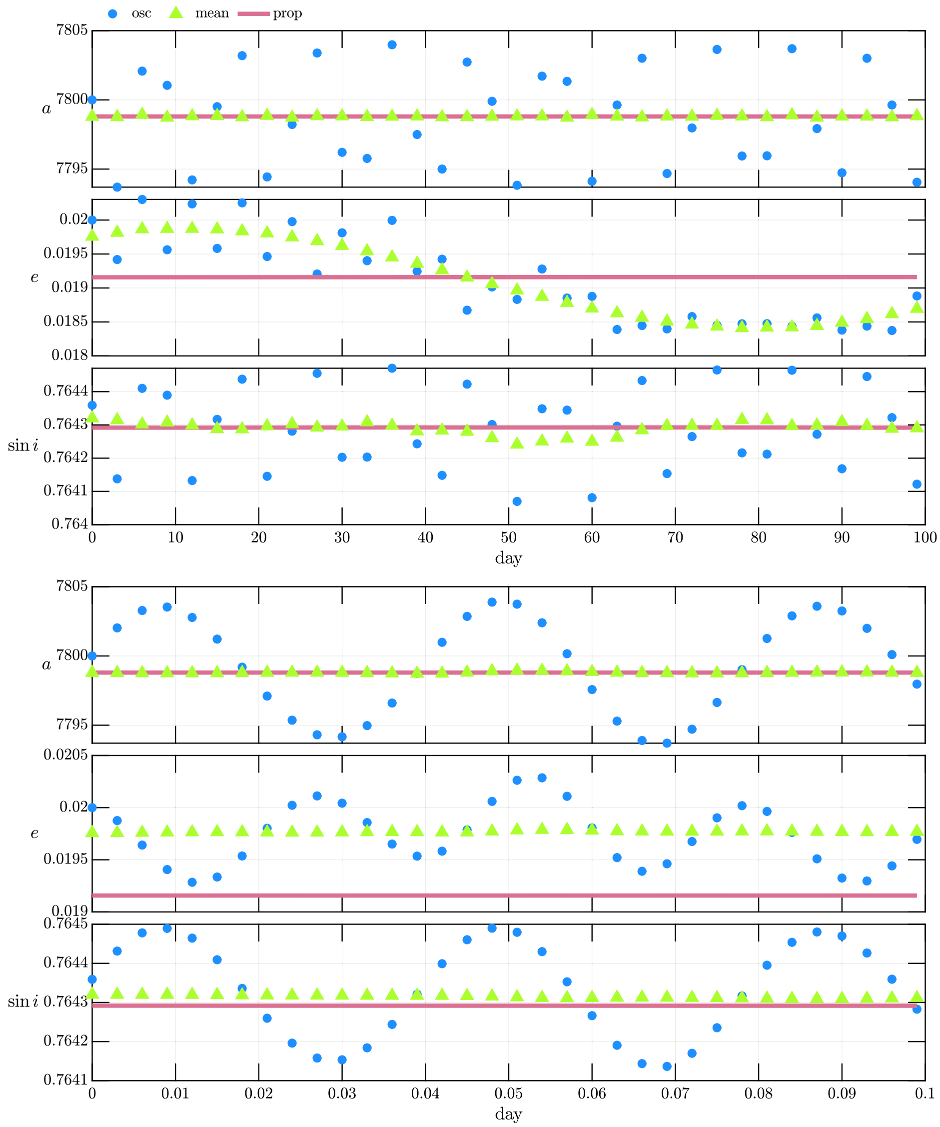

Fig. 3. Osculating, mean, and proper elements comparison for a satellite in low-Earth orbit, over a 100-day evolution (*top*) and 0.1-day evolution (*bottom*). The osculating elements time series is generated from a model composed of 10×10 Earth-gravity harmonics, lunisolar, SRP, and drag perturbations. The initial osculating elements are $a = 7800$ km, $e = 0.02$, $i = 49.85^{\circ}$, $\Omega = 20^{\circ}$, $\omega = 60^{\circ}$, and $M = 80^{\circ}$. The model used in converting from the osculating state to the corresponding mean and proper elements is the same.

object's proper-elements calculation, we include it in the truncated model. This operation is not only for model completeness, but also for a numerical way of including drag in the proper-elements calculation, taking advantage of the ad hoc natural of the Ptolemy method. This procedure could be extended to orbits more affected by drag, however quantifying the performance would require further study. Nevertheless, for objects affected significantly by drag in LEO, we recommend excluding drag in the truncated model and examining the natural evolution of proper elements under drag. The proper elements would evolve in the similar fashion as their osculating and mean elements counterparts, but in a less oscillating fashion as proper elements describe the long-term, fully averaged evolution.

4. Proper elements in orbital-maneuver characterization.

A maneuvering satellite is indicative of a change in status and could potentially signal a threat. Quickly determining that a satellite has maneuvered is thus a high priority for space sustainability and domain awareness. Many geosynchronous satellites are using long duration, low-thrust maneuvers for station keeping. OneWeb, SpaceX, and Amazon moreover, have each launched ambitious plans to place hundreds to thousands of satellites in LEO, where subsequent orbit raising and de-orbiting maneuvers will be accomplished using low-thrust propulsion (Byers and Boley, 2023). The current methods for maintaining the space-object catalog cannot automatically deal with such cases. High-impulse maneuvers generally

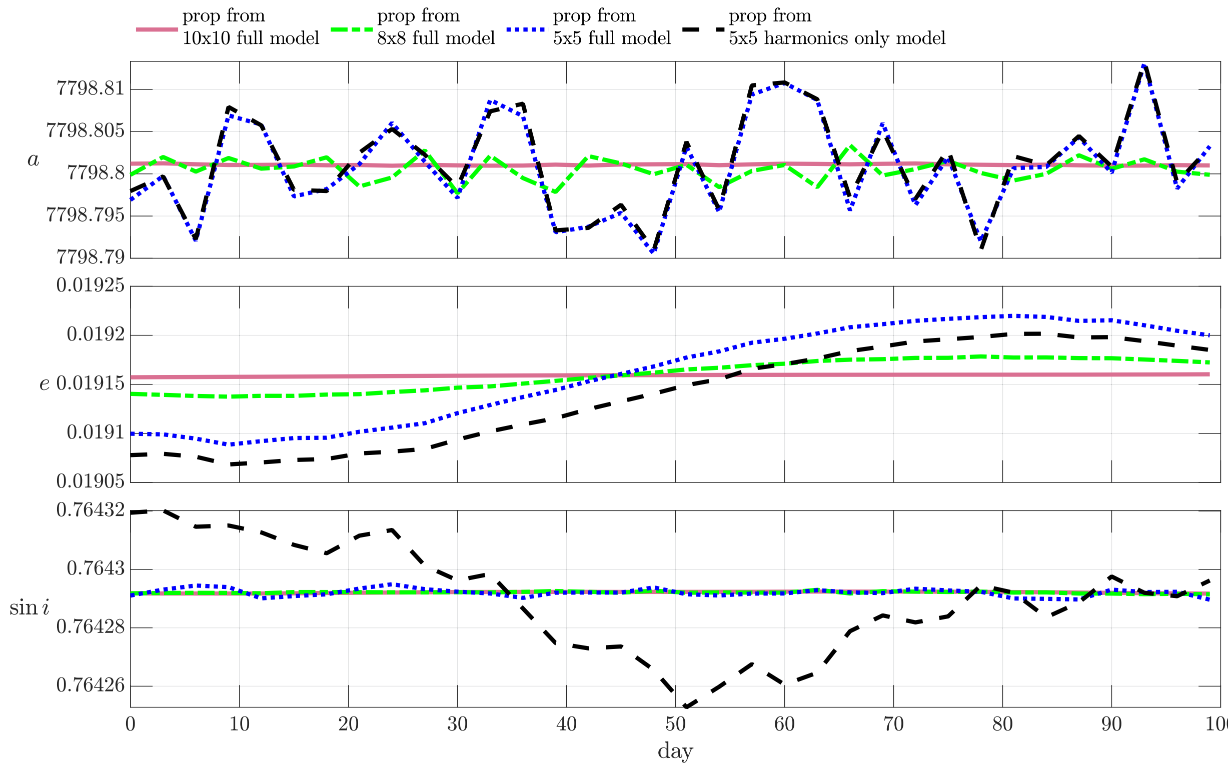

Fig. 4. Proper elements converted from multiple truncated models representing different model fidelity. The simulated osculating orbital elements are obtained from a model composed of 10×10 Earth-gravity harmonics, lunisolar, SRP, and drag perturbations with initial osculating elements $a = 7800$ km, $e = 0.02, i = 49.85^\circ, \Omega = 20^\circ, \omega = 60^\circ$, and $M = 80^\circ$. Over which, proper elements are computed based on different levels of model truncation. The *solid line* is computed from the same model as the osculating orbital elements; the *dash-dot line* is from a reduced 8×8 Earth-harmonics model, including all other gravitational and non-gravitational perturbations; the *dotted line* is from a further reduced 5×5 Earth-harmonics model; and the *dash line* is from a 5×5 Earth-harmonics-only model.

result in observations that are outside the error bounds and the object becomes an uncorrelated track. Low-impulse maneuvers are often not detected as the maneuvers are not large enough to result in the observations being outside the error box; consequently, the orbit determination fits through the maneuver. Subsequent analysis of element change may indicate a maneuver (Kelecy et al., 2007; Lemmens and Krag, 2014b; Lemmens and Krag, 2014a), but the current system will not likely detect such a maneuver. Methods based simply on mean elements require fine tuning of the algorithm parameters and are skewed by noise statistics. Here, we investigate whether proper elements provide a more robust quantification of a maneuver than induced changes in mean element.

We focus on the different performance under various maneuvers for proper elements and mean elements. Osculating elements, being more prone to the highly nonlinear dynamics, perform generally worse than mean elements. Maneuvers in along-track and cross-track directions in the instantaneous RSW frame are simulated to introduce changes in eccentricity and inclination evolution. While the maneuver magnitudes and directions are randomly selected, their absolute values are generally rather small ($<\approx 100$ mm/s $= 10$ cm/s). It is clear to see that for proper eccentricity and proper sine of inclination in Fig. 5 and Fig. 6, the maneuvers are perspicuous with non-crossing in between pre-maneuver phase and post-maneuver phase. The performances for mean eccentricity and mean inclination are more muddled than their proper counterparts. Although in a vertical comparison, we could still recover the different maneuvers, considering a single time series, there is no profound shape-wise difference between any time series with maneuver and those without; furthermore, the time series with different maneuvers have shapes so similar that it is also hard to distinguish among themselves.

Conceptually, the clearer performance in response to maneuvers by proper elements could be explained by its “quasi-constant” feature. Consider the last pre-maneuver data point, all those beforehand, in proper-elements space, are the same so the evolution appears as a single line in the pre-maneuver phase; while for the first post-maneuver data point, all subsequent data appear the same, thus performing as “quasi-constant” again. There should always be a difference between the last pre-maneuver data point and the first post-maneuver data point in the existence of a maneuver, thus creating a performance similar to a perfect step response. Moreover, we should mention that the nonlinear dynamics still exist, but proper elements have incorporated this dynamics into their values because of their intrinsic dynamical connection with the initial conditions in the long-term evolution.

However, the explanation is partial as it omits the effects of the change induced by a maneuver in each set of orbital

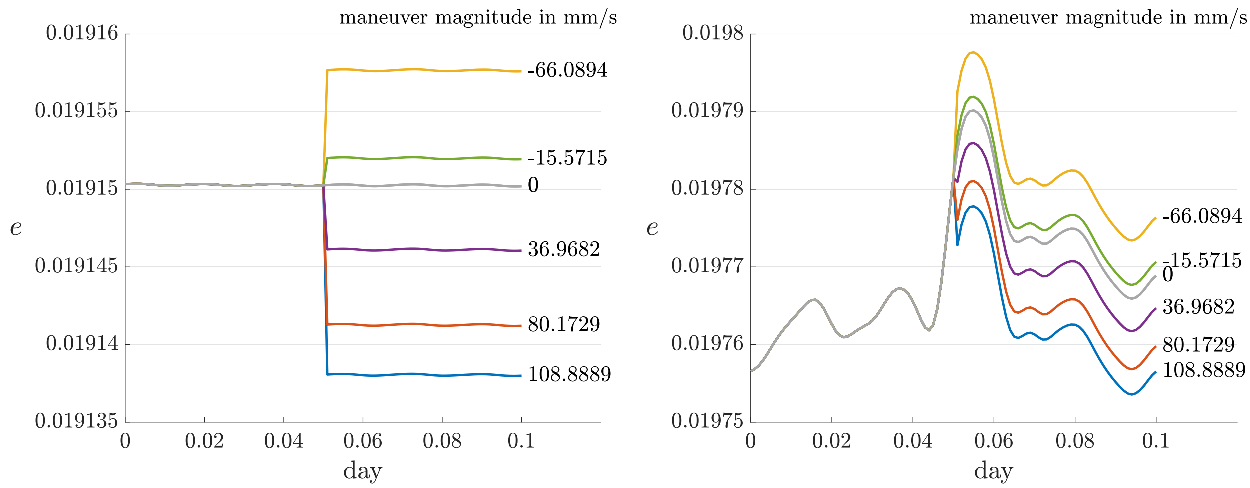

Fig. 5. The proper (*left*) and mean (*right*) eccentricity evolution under the maneuvers of multiple magnitudes in the along-track/S direction in the RSW frame defined at the maneuver instance. Maneuver magnitude is noted at the end of each time series in mm/s. The initial osculating elements are $a = 7800$ km, $e = 0.02, i = 49.85^\circ, \Omega = 20^\circ, \omega = 60^\circ$, and $M = 80^\circ$. The simulated osculating orbital elements are obtained from a model composed of 50×50 Earth-gravity harmonics, lunisolar, SRP, and drag perturbations.

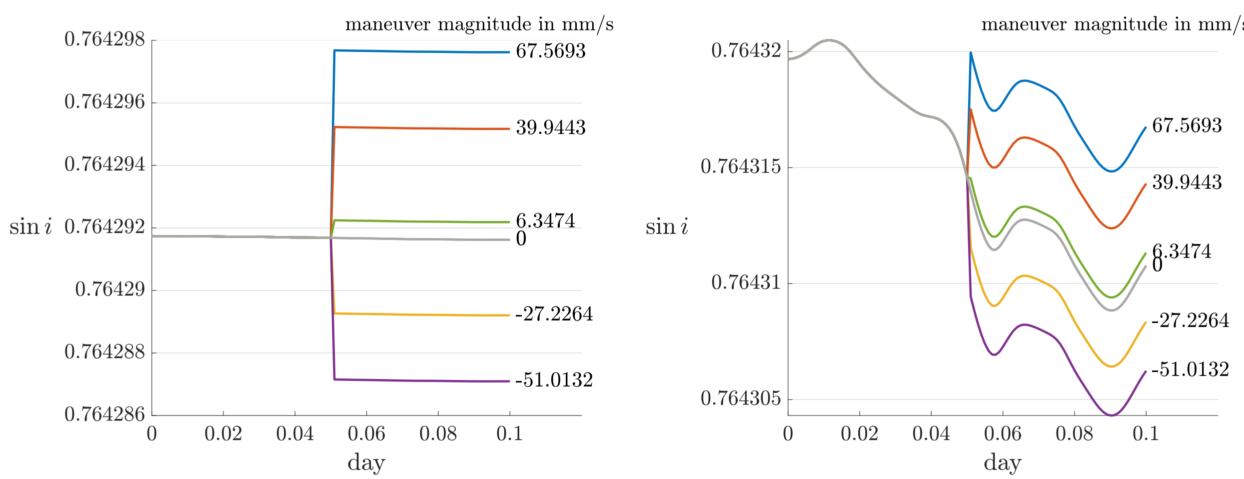

Fig. 6. The proper (*left*) and mean (*right*) sine of inclination evolution under the maneuvers of multiple magnitudes in the cross-track/W direction in the RSW frame defined at the maneuver instance. Maneuver magnitude is noted at the end of each time series in mm/s. The initial osculating elements are $a = 7800$ km, $e = 0.02, i = 49.85^\circ, \Omega = 20^\circ, \omega = 60^\circ$, and $M = 80^\circ$. The simulated osculating orbital elements are obtained from a model composed of 50×50 Earth-gravity harmonics, lunisolar, SRP, and drag perturbations.

elements. So we define a statistics value — change over standard deviation (COSD) — to quantify the maneuver response performance. COSD is defined as the ratio of the absolute value change induced by a maneuver over the standard deviation of the pre-maneuver time series. The induced change is simply the difference between the post-maneuver state value and the pre-maneuver one. A large COSD value means a maneuver would induce a large jump relative to the pre-maneuver history and it would be more certain to assert the value change to be irrelevant to the time-series' natural oscillation.

With the definition of COSD, we could assure that if the maneuver response performance from proper elements and mean elements are the same, they should have the same COSD value. And by assigning the x-axis to proper elements and y-axis to mean elements, if the performances are the same, there will be an equal-performance line as the COSD values for proper elements and mean elements are the same along this line as indicated by the dashed line in Fig. 7. Yet, if proper elements are performing better than mean elements under the same maneuver, the COSD value for proper elements is going to be larger than for mean elements, thus a data point lying higher than the equal-performance line.

In Fig. 7, each data point has the x-component as COSD value for mean elements and y-component as COSD value for proper elements. The *dot point* is for cross-track maneuver, thus related with proper sine of inclination, and *triangle point* is for along-track maneuver, thus related with proper eccentricity. The number on top of

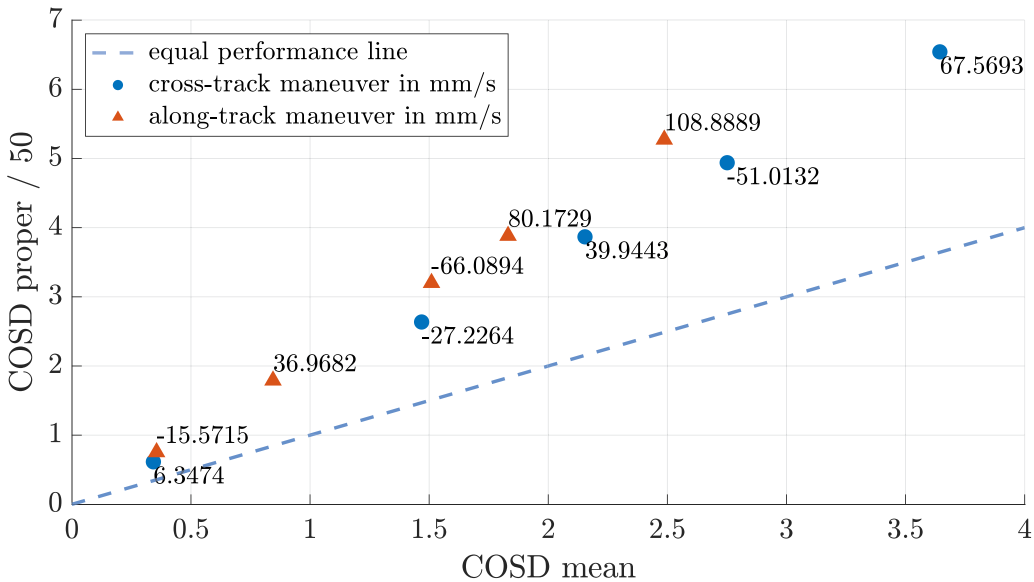

Fig. 7. The comparison of the COSD values for proper- and mean-elements evolutions under multiple cross-track (*dot*) and along-track (*triangle*) maneuvers. Maneuver magnitude is noted next to each point. The x-axis represents the COSD value for mean-elements evolution. The y-axis is the COSD value for proper-elements evolution divide by 50, manually decreasing its value for illustration purpose. The *dotted line* is the equal-performance line after scaling down COSD value for proper elements by 50. Points higher than the equal-performance line have a larger y-axis value than x-axis'. COSD values for proper-elements evolutions are all larger than those for mean elements from the same magnitude. This visualizes the better performance of proper elements in characterizing maneuvers than mean elements.

each data point is the corresponding maneuver magnitude in mm/s. We could verify that the COSD value for proper elements is larger than the COSD value for mean elements under the same maneuver as all of the data points locate above the equal-performance line. In fact, COSD value for proper elements is so much larger than COSD value for mean elements, we have to scale down the axis for COSD value for proper elements by 50 times for visual inspection, otherwise the dotted equal-performance line would be almost overlaying with the x-axis in the plots. This is essentially saying that if we increase mean elements performance by 50 times, it would still not match the proper elements' performance.

We focus our analysis on the performance for small-magnitude maneuvers. Since the COSD values for the smallest maneuvers in both eccentricity and inclination lie much higher above the equal-performance line, we could easily verify the better performance of proper elements. So we could conclude without the lose of generality that if a maneuver could be clearly shown by mean elements, it would be shown by proper elements in a better fashion; if a maneuver could not be shown by proper elements, it would be impossible for mean elements to show this maneuver. This conclusion should be useful in designing state representation for orbital maneuver-detection algorithms and researches.

Moreover, by using the data point's perpendicular distance to the equal-performance line as an indicator for performance change due to different maneuver magnitude in Fig. 7, we could observe that the larger a maneuver is, the more profoundly clear it would be for proper elements to illustrate the maneuver, because the data point for that maneuver magnitude lies higher above the equal-performance line than a data point for a relatively smaller maneuver magnitude. In fact, comparing to the equal-performance-line's slope, the data points for different maneuver magnitudes create a steeper line with a larger slope, this illustrates the same performance that could be found in Fig. 5 and Fig. 6: while the changes in mean elements are not profoundly different for increasingly larger maneuver magnitudes, the changes in proper elements are increasingly visible.

5. Proper elements in maneuver detection and limitations

We have shown how proper elements could characterize orbital maneuvers. We have further provided a general statistic to quantify proper-elements' performance as a state representation for the same purpose. Moreover, we explained proper elements' quantified performance and its linkage with the unique "quasi-constant" feature. Here, we develop the detection mechanism based on the unique orbital signatures they provide and show the limitations of proper elements in orbital-maneuver detection.

In a realistic detection scenario, an online detection is most desired, meaning that we want to determine that a maneuver has occured as soon as it happens rather than having to conduct a posterior analysis with an increasing amount of post-maneuver data. Taking this preference into account, we adopt the Bayesian online changepoint-detection (BOCD) algorithm. With proper elements as our state, as analyzed in Section 4, a maneuver is reflected as a state change and the place where this maneuver happens is the changepoint in the evolution. We would be able to detect the changepoint by applying BOCD into the time series of proper elements. For the detailed explanation of BOCD algorithm, we direct the reader to its original paper (Adams and MacKay, 2007). The BOCD algorithm estimates the posterior distribution over the "run length" defined as the accumulated time since the last changepoint. The basic idea behind BOCD is to model the data using a probabilistic framework and calculate the posterior probability of a changepoint occurring at each time step. A changepoint is a location in the sequence where a change is hypothesized to have occurred. BOCD algorithm calculates each state's posterior probability of having every possible run lengths based on data up to that state; from these posterior probabilities calculated, whether that state is a changepoint or a continuum of previous data could be determined.

Here, we present the results from the BOCD algorithm. We focus on maneuver magnitudes that could be detected in application and we expect the maneuver detection is pinpointed as soon as it happens. Although there could be case-to-case differences, we could generally detect maneuvers at the fine-tuning magnitude of around twenty millimeter per second (∼20 mm/s). Fig. 8a is the BOCD detection result on the top of proper-eccentricity evolution under 7 maneuvers. The *dash lines* are used to mark the known maneuvers and *solid lines* the detected maneuvers. There are 8 segments separated by 7 maneuvers. Within each segment, proper elements are quasi-constant due to the lack of maneuver. Between segments, a maneuver creates a "jump" between the two segments, the same performance as shown in Fig. 5. BOCD is able to detect these "jumps". We also notice that a large maneuver does not necessarily equate to a large "jump" as the "jump" magnitude is also affected by the state where the maneuver occurs.

BOCD uses a Bayesian approach to quantify the likelihood of a changepoint at each time step. It starts with an initial prior distribution, which expresses the belief about the absence of changepoints. Gaussian distribution or exponential family is the most common distribution that has been tested in BOCD research (Adams and MacKay, 2007). Besides being validated for BOCD application, modeling a proper-elements sequence between maneuvers as a Gaussian distribution, as shown in the histogram representation in Fig. 8b, captures the quasi-constancy of proper elements. Maneuvers result in the changes of proper elements and thusthe changes of histogram distributions. This is the fundamental reason for the application of BOCD. We fit the proper-elements data in a segment with a normal distribution and show the fitted distribution on

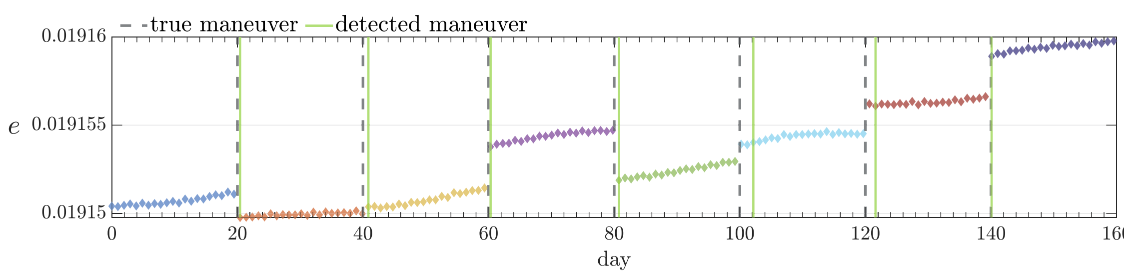

(a) A maneuver-detection scenario from employing BOCD on a proper-eccentricity time series. The *solid lines* represents the detected maneuvers and the *dashed lines* are the true maneuvers. The maneuvers are uniformly applied in the along-track/S direction with random magnitudes following a Gaussian distribution with a 20mm/s mean. The minimum magnitude in these maneuvers is 14.8713 mm/s and the maximum is 23.4958 mm/s.

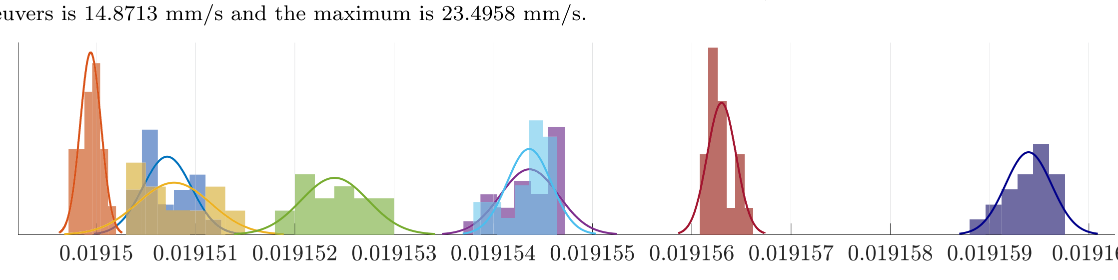

(b) The histogram illustration of the proper-eccentricity evolution between maneuvers. The maneuver-induced jumps in proper-eccentricity time series are characterized by the distribution shifts. Each colored group of histograms corresponds to a segment in the proper-eccentricity evolution with the same color. We fit a normal distribution over each group of histograms and plot the fitted bell-shape curves on the top.

Fig. 8. A maneuver-detection scenario in proper eccentricity (*top*) and its histogram illustration (*bottom*). The detected maneuvers come from employing BOCD on the proper-eccentricity time series. The groups of histogram and the fitted bell-shape curves correspond to the segments in the proper-eccentricity evolution with the same colors. The initial osculating elements are $a = 7800$ km, $e = 0.02, i = 49.85^\circ, \Omega = 20^\circ, \omega = 60^\circ$, and $M = 80^\circ$. The simulated osculating orbital elements are obtained from a model composed of 40×40 Earth-gravity harmonics, lunisolar, SRP, and drag perturbations. The conversion to the proper elements uses the same model.

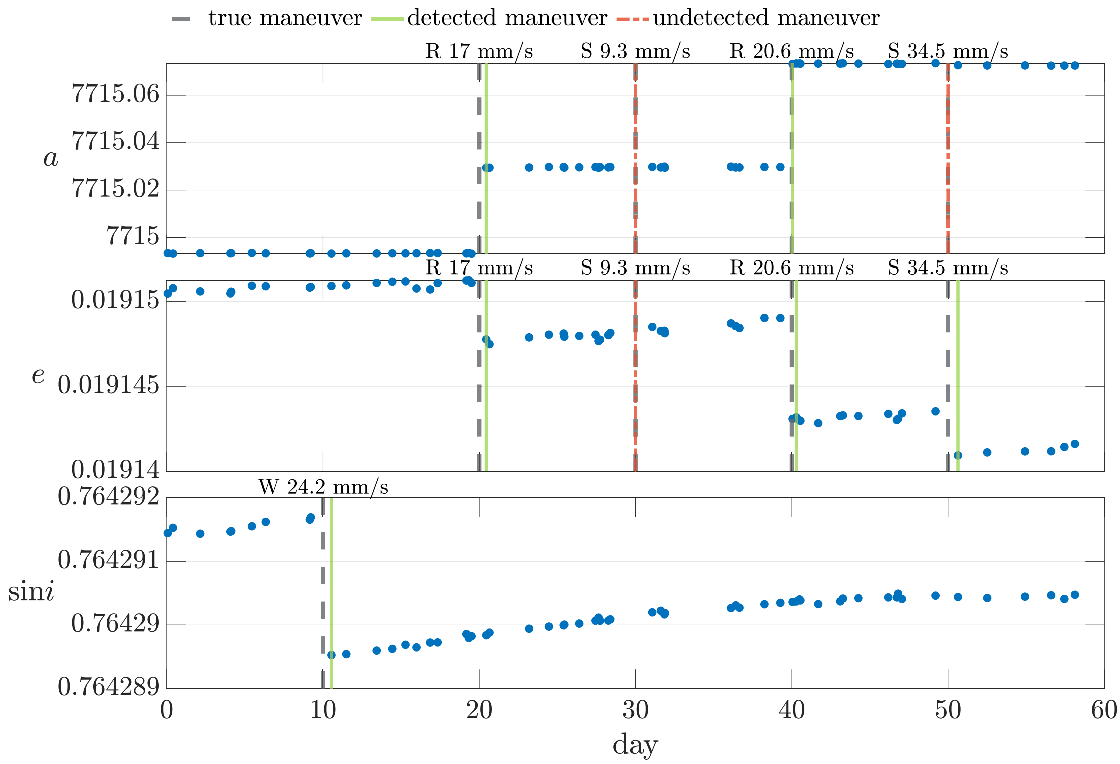

Fig. 9. A maneuver detection scenario with nonuniform data acquisition rate and random maneuver magnitudes and directions. The *dashed lines* are the true maneuvers; the *solid lines* the detected maneuvers; the *dash-dot lines* the undetected maneuvers. While the maneuver magnitudes and directions are randomized, the observed data is archived randomly in time. At roughly 1 data per day, we simulate an ideal TLE data acquisition rate. We detect almost all maneuvers except for a small one at day 30. Proper eccentricity detects the S direction maneuver at day 50 where proper semimajor axis misses. The initial osculating elements are $a = 7800$ km, $e = 0.02, i = 49.85^\circ, \Omega = 20^\circ, \omega = 60^\circ$, and $M = 80^\circ$. The simulated osculating orbital elements are obtained from a model composed of 40×40 Earth-gravity harmonics, lunisolar, SRP, and drag perturbations. The conversion to the proper elements uses the same model.

top of the corresponding histograms in the same color. The distribution segments are numbered sequentially. As the maneuver directions are randomized, with a negative along-track direction, the distribution shifts leftwards along the eccentricity axis, and with a positive along-track direction, the distribution shifts rightwards. This follows the insights from Gauss' variational equations of motion. As we convert a maneuver's effect from a time-sequence change to a distribution change in the proper-elements domain, we naturally employ Bayesian analysis and the BOCD algorithm.

Furthermore, we generate a more realistic scenario with random maneuvers and randomized observation state converted proper elements in Fig. 9. The states are sampled randomly in time at roughly 1 data per day (an ideal TLE data-acquisition rate). Maneuver directions and magnitudes are randomized by a normal distribution with mean value at 20 mm/s and variance at 5 mm/s. The maneuvers are generated every 10 days and they are: at day 10, W direction with a magnitude of 24.2 mm/s; at day 20, R direction with a magnitude of 17.0 mm/s; at day 30, S direction with a magnitude of 9.3 mm/s; at day 40, R direction with a magnitude of 20.6 mm/s; at day 50, S direction with a magnitude of 34.5 mm/s. The W direction would only change proper sine of inclination while R or S direction could induce changes in proper semi-major axis and proper eccentricity. However, the maneuver magnitude and pre-maneuver state would decide how much the change would be. There could be the case, even theoretically, that a maneuver in S direction would not induce change in proper semi-major axis. This is why we need all three proper elements for a complete maneuver detection.

We detect almost all the maneuvers with only one S direction maneuver missed at day 30 due to its small magnitude. The detection is ideal as we always find the data point right after the true maneuver as our detected maneuver. This performance accounts for the quasi-constant feature of proper elements. As analyzed herein, proper elements are quasi-constant without maneuver and when a maneuver is implied the state shift is so distinctive that it would appear like a “jump”. We also notice that for 34.5 mm/s S-direction maneuver at day 50, the detection is achieved in proper eccentricity. In this case, proper semi-major axis does not show a state change.

6. Conclusion

Space situational and domain awareness (SSA and SDA) are crucial to maintain a safe circumterrestrial space environment. Among the challenges is the dynamics ambiguity coming from the highly nonlinear astrodynamics. This research aims at proposing and introducing proper elements for this challenge and elevating the importance of dynamics modeling. The Ptolemy method is constructed as a general numerical scheme to calculate proper elements. After examining and discussing its performance in calculating asteroid proper elements, we extend its application in calculating RSO proper elements. The dynamical connection between proper elements and seminal works on satellite long-term eccentricity and inclination motions is provided in Appendix A. The model reduction nature in those works and the effect of increasing model sophistication and complexity on proper elements are discussed in detail. After creating a full comparison among osculating elements, mean elements, and proper elements for a RSO, we further our investigation on the effect of model fidelity over the quality of proper elements, according to the multi-level fidelity discussion in the analytical works done in Appendix A. While explaining desired proper-elements performance, we introduce the unique "quasi-constant" feature of proper elements. By applying this feature, we explain the superior performance shown by proper elements in orbital-maneuver characterization. We also propose a novel statistical quantity, COSD, as a criteria for the performance comparison.

This work presented proper elements as a state representation for RSOs and cleared the conceptual barrels for further application. With the "quasi-constant" feature, we have already shown its application in orbital maneuver among many other possible applications in SSA/SDA. In this work, the concept of proper elements that originates from asteroid dynamics has been assigned a renewed content and could potentially provide many advantages in research concerning RSOs with its unique physical and dynamical qualities.

The preceding analyses, however, ignore the effects of resonances, and chaotic diffusion resulting from resonant phenomena which can cause significant changes in the proper elements (Migliorini et al., 1998; Morbidelli, 2002). Non-gravitational perturbations can also have important implications, such as the Yarkovsky-driven drift in proper semi-major axis (Bottke et al., 2006). All of these subtleties and nuances will be relevant for the circumterrestrial context. A potential limitation with man-made RSOs is that non-gravitational affects tend to be larger than the small-body problem, and such radiation and drag perturbations can behave as de-correlators of common space events. This represents a basic question we will explore in great detail in the future work.

In our current work, we focused on validating the application of proper elements for maneuver detection. Rather than dealing with the complex, systematical data-acquisition and tracking issues, we simulate the states directly in a high-fidelity model with known maneuvers. In such a way, we focus directly on proper element and its application on maneuver detection. The tracking association, despite being out of the scope of our current work, would be a fruitful direction for future development. We are also interested to see if conducting track association under the scope of proper elements in combination with multiple hypothesis testing would provide any advantages in defining the likelihood of the origins of new track. In addition, it would be valuable to expand our current work to include maneuver estimation on top of successful maneuver detection.

Declaration of Competing Interest

The authors declare that they have no known competing financial interests or personal relationships that could have appeared to influence the work reported in this paper.

Acknowledgments

We are grateful to Boulat Bash, of the University of Arizona, for his introduction on the classical detection and estimation theory. AR acknowledges support by the Air Force Office of Scientific Research (AFOSR) under Grant No. FA9550-21-1-0191.

Appendix A. Proper elements in dynamical models of multi-level fidelity

A.1. Simplified Earth zonal-harmonics dynamics

Following Cook (1966), Walter (2018), and Chao and Hoots (2018), under the small eccentricity assumption, i.e., $e \ll 1$, the governing system of differential equations for the components of the mean (orbit-averaged) projected eccentricity vector $\boldsymbol{e} = (\eta, \xi) = (e\sin\omega, e\cos\omega)$, under Earth harmonics J_2 and J_3, is given as

$$\dot{\eta} = 3J_2\left(\frac{\mu}{a^3}\right)^{1/2}\left(\frac{R}{a}\right)^2\left(1-\frac{5}{4}\sin^2 i\right)\xi, \tag{A.1}$$

$$\begin{aligned}\dot{\xi} = &-3J_2\left(\tfrac{\mu}{a^3}\right)^{1/2}\left(\tfrac{R}{a}\right)^2\left(1-\tfrac{5}{4}\sin^2 i\right)\eta \\ &+\tfrac{1}{6}\left(\tfrac{\mu}{a^3}\right)^{1/2}J_3\left(\tfrac{R}{a}\right)^3 P_3^1(0)P_3^1(\cos i).\end{aligned} \tag{A.2}$$

From the associated Legendre function, we have $P_3^1(0) = 3/2$, $P_3^1(\cos i) = \frac{3}{2}(1-5\cos^2 i)(1-\cos^2 i)^{1/2}$. We also adopt the shorthand expression $f = \sin^2 i$, as used in Cook (1966), so that the system of different equations becomes

$$\begin{aligned}\dot{\eta} &= 3J_2\left(\tfrac{\mu}{a^3}\right)^{1/2}\left(\tfrac{R}{a}\right)^2\left(1-\tfrac{5}{4}f\right)\xi, \\ \dot{\xi} &= -3J_2\left(\tfrac{\mu}{a^3}\right)^{1/2}\left(\tfrac{R}{a}\right)^2\left(1-\tfrac{5}{4}f\right)\eta \\ &\quad -\tfrac{3}{2}\left(\tfrac{\mu}{a^3}\right)^{1/2}J_3\left(\tfrac{R}{a}\right)^3\left(1-\tfrac{5}{4}f\right)\sin i.\end{aligned} \tag{A.3}$$

The projected eccentricity vector can be converted to eccentricity and argument of perigee by the relations $e = \sqrt{\xi^2+\eta^2}$ and $\tan\omega = \eta/\xi$.

The dynamics shown in Eq. A.3 is a set of non-divergent, linear differential equations for a 2D harmonic oscillator. The solution is given by

$$\begin{aligned} \eta - e_f &= e_p \sin(n_p t + \phi_p), \\ \xi &= e_p \cos(n_p t + \phi_p). \end{aligned} \tag{A.4}$$

The parameters e_f and n_p are determined by the zonal harmonics J_2 and J_3, as well as the orbit semi-major axis a and equatorial inclination i; the parameters e_p and ϕ_p are determined by J_2, J_3, a, i, and the initial eccentricity e_0 and initial argument of perigee ω_0; all parameters e_f, e_p, n_p, ϕ_p in this simplified dynamical model are constant. The meaning behind this solution, Eq. A.4, is that, in the plane of (η, ξ), the evolution of a satellite's eccentricity vector $\boldsymbol{e}$ can be decomposed as a summation of a constant vector, called the forced eccentricity vector and denoted as $\boldsymbol{e}_f = [0, e_f]$, and a rotating vector with constant magnitude and rotation speed, called the proper eccentricity vector, $\boldsymbol{e}_p = [e_p \sin(n_p t + \phi_p), e_p \cos(n_p t + \phi_p)]$.

The magnitudes of vectors $\boldsymbol{e}_f$ and $\boldsymbol{e}_p$ are constant, but slightly different in their implications. The forced eccentricity e_f is decided by the dynamics, while the proper eccentricity e_p, besides being influenced by the dynamics, is also related to the initial condition. This means that for different space objects, as long as their semi-major axis a and inclination i are the same, they will share the same forced eccentricity vector, as this vector is "forced" by the dynamical environment. On the other hand, for each RSO, with its own unique e_0, ω_0 initial state, e_p is constant throughout its forward and backward time evolution. But for RSOs with different initial e_0, ω_0, their e_p values will differ, and there will be no situation in the past or future such that their e_p will ever share the same value, so that each space object could have a "proper" branding by its e_p value.

We verify the constancy of proper eccentricity under the simplified dynamics, specified by Eq. A.3, in Fig. A.10 (*top-left panel*). With a given semi-major axis and inclination, we calculate the frozen eccentricity and take the vector difference, as in Rosengren et al. (2019a), to get the proper eccentricity. We term the proper elements obtained from this general vector operation method the analytical Cook proper elements. Being at the same magnitude level as MATLAB's minimum distance for difference discrimination at the magnitude of ~0.05, the range of proper eccentricity oscillations is small enough to be declared constant to machine precision.

A.2. Brouwer-Lyddane secular elements

Brouwer's solution to the zonal-harmonics problem (Brouwer, 1959) is arguably more complete than that of Cook (1966), as it treats both the first- and second-order secular perturbations, as well as the first-order short-periodic (related to the satellite's mean motion) and long-periodic (related to the evolution of the argument of the perigee) perturbations of the orbital elements. Lyddane (1963) reformulated Brouwer's solution using Poincaré variables to free it of the mathematical singularities associated with circular or equatorial orbits that otherwise pla-

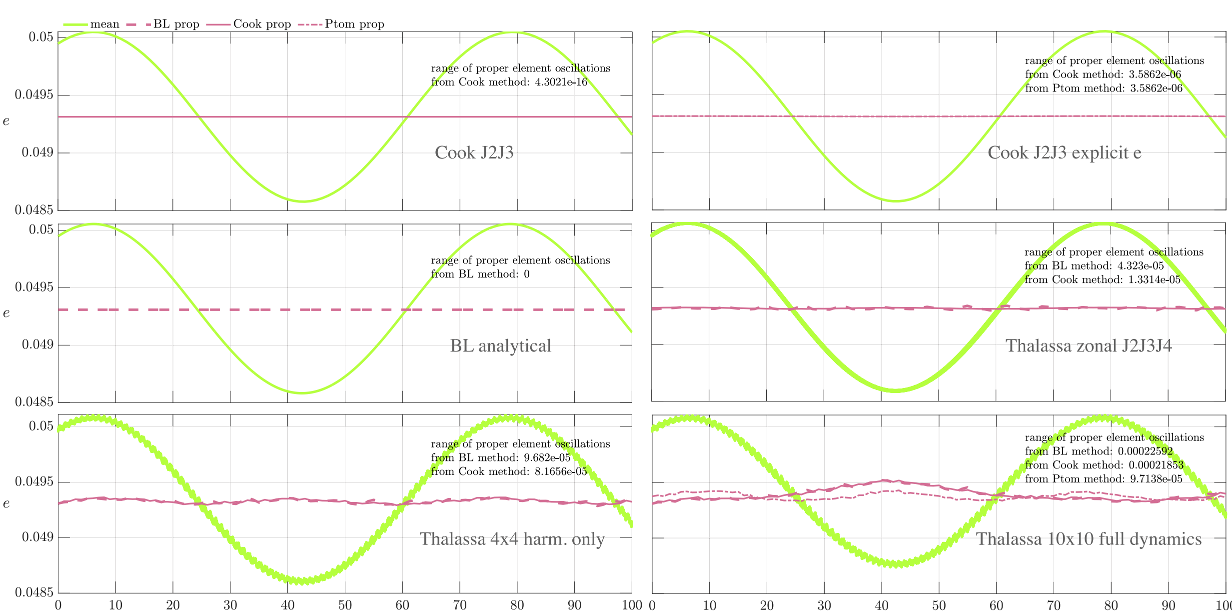

Fig. A.10. Mean and proper eccentricities under a hierarchy of dynamical models and various computational methods. The range of proper-element oscillations is shown as an indicator of constancy. The initial mean elements in all cases are $a = 7180.5142$ km, $e = 0.049948, i = 45.0096°, \Omega = 44.9754°, \omega = 59.7801°$, and $M = 211.2366°$. The mean element evolution for the *top panels* are from Eqs. A.3 and A.12, respectively. The mean-elements in the *middle-right panel* is from Brouwer-Lyddane's analytical formulation. In the remaining panels, THALASSA (Amato et al., 2019), an open-source, high-accuracy, and fast orbit propagator, for RSOs long-term propagation, is used to propagate the osculating dynamics under the various dynamical models, and its output is numerically converted int.o mean elements.

gue the classical equations written in Keplerian or Delaunay elements. Lyddane further pointed out that "the sum of Brouwer's long-period and short-period terms, [is] not necessarily the difference between [the osculating and secular elements]." As noted earlier, the secular elements are the proper elements under the corresponding model and theory that built them. Fig. A.10 (*middle-left panel*) shows the evolution of the mean and proper/secular elements according to Brouwer's analytical solution, where the latter are theoretically (and numerically) constant under the assumed dynamical model.

We can further illustrate the connection between Cook's proper elements and Brouwer's secular elements by adopting the underlying assumptions of Cook (1966) within Brouwer-Lyddane's (BL's) treatment. We employ the nomenclature of Brouwer (1959), where single primed variables represent the long-periodic terms and double primed variables are used for the secular variations. Following Cook, we recast Brouwer's solution in terms of $\xi = e\cos g$, $\eta = e\sin g$, where the Delaunay g is equivalent to the argument of perigee. For the mean (secular plus long-periodic) elements, we can write (Brouwer, 1959; Lyddane, 1963; Davenport, 1965)

$$\begin{aligned}\eta &= e\sin g = (e'' + \delta e)\sin g'' + e''\delta g\cos g'',\\ \xi &= e\cos g = (e'' + \delta e)\cos g'' - e''\delta g\sin g'',\end{aligned} \tag{A.5}$$

where

$$\begin{aligned}\delta e = &\left\{\frac{1}{8}\gamma_2 e'' v^2\left[1 - 11\theta^2 - 40\theta^4\left(1-5\theta^2\right)^{-1}\right]\right.\\ &\left.-\frac{5}{12}\frac{\gamma_4'}{\gamma_2'}e'' v^2\left[1 - 3\theta^2 - 8\theta^4\left(1-5\theta^2\right)^{-1}\right]\right\}\cos 2g''\\ &+\left\{\frac{1}{4}\frac{\gamma_3'}{\gamma_2'}v^2\sin i'' + \frac{5}{64}\frac{\gamma_5'}{\gamma_2' v^2}\sin i''\left(4+3e''^2\right)\left[1 - 9\theta^2 - 24\theta^4\left(1-5\theta^2\right)^{-1}\right]\right\}\sin g''\end{aligned} \tag{A.6}$$

$$\begin{aligned}\delta g = &\left\{-\tfrac{1}{16}\gamma_2'\left[(2+e''^2) - 11(2+3e''^2)\theta^2 - 40(2+5e''^2)\theta^4\left(1-5\theta^2\right)^{-1}\right.\right.\\ &\left.-400e''^2\theta^6\left(1-5\theta^2\right)^{-2}\right] + \tfrac{5}{24}\tfrac{\gamma_4'}{\gamma_2'}\left[2 + e''^2 - 3(2+3e''^2)\theta^2 - 8(2+5e''^2)\theta^4\left(1-5\theta^2\right)^{-1}\right.\\ &\left.\left.-80e''^2\theta^6\left(1-5\theta^2\right)^{-2}\right]\right\}\sin 2g'' + \left\{\tfrac{1}{4}\tfrac{\gamma_3'}{\gamma_2'}\left(\tfrac{\sin i''}{e''} - \tfrac{e''\theta^2}{\sin i''}\right) + \tfrac{5}{64}\tfrac{\gamma_5'}{\gamma_2'}\right.\\ &\times\left[\left(\tfrac{v^2\sin i''}{e''} - \tfrac{e''\theta^2}{\sin i''}\right)(4+3e''^2) + e''\sin i''(26+9e''^2)\right]\left[1 - 9\theta^2 - 24\theta^4\left(1-5\theta^2\right)^{-1}\right]\\ &\left.-\tfrac{15}{32}\tfrac{\gamma_5'}{\gamma_2'}e''\theta^2\sin i''(4+3e''^2)\left[3 + 16\theta^2\left(1-5\theta^2\right)^{-1} + 40\theta^4\left(1-5\theta^2\right)^{-2}\right]\right\}\cos g''\\ &+\left\{-\tfrac{35}{1152}\tfrac{\gamma_5'}{\gamma_2'}\left[e''\sin i''(3+2e''^2) - \tfrac{e''\theta^2}{\sin i''}\right]\left[1 - 5\theta^2 - 16\theta^4\left(1-5\theta^2\right)^{-1}\right]\right.\\ &\left.+\tfrac{35}{576}\tfrac{\gamma_5'}{\gamma_2'}e''^3\theta^2\sin i''\left[5 + 32\theta^2\left(1-5\theta^2\right)^{-1} + 80\theta^4\left(1-5\theta^2\right)^{-2}\right]\right\}\cos 3g''.\end{aligned} \tag{A.7}$$

Here, $\theta = \cos i''$, $\gamma_2 = \frac{k_2}{a''^2}$, $\gamma_4 = \frac{k_4}{a''^4}$, $\gamma_3 = \frac{A_{3,0}}{a''^3}$, $\gamma_5 = \frac{A_{5,0}}{a''^5}$, $\gamma_i' = \gamma_j v^{-2j}$, $v = (1-e''^2)^{\frac{1}{2}}$. From Davenport (1965), we note that $k_2 = \frac{1}{2}J_2R^2$, $k_4 = -\frac{3}{8}J_4R^4$, $A_{3,0} = -J_3R^3$, $A_{5,0} = -J_5R^5$, where R is Earth's equatorial radius.

Treating the eccentricity and inclination as small parameters, and considering only the J2 and J3 zonal dynamics, we find:

$$\begin{aligned}\delta e &= \frac{1}{4}\frac{\gamma_3'}{\gamma_2'}\sin i''\sin g'',\\ e''\delta g &= \frac{1}{4}\frac{\gamma_3'}{\gamma_2'}\sin i''\cos g''.\end{aligned} \tag{A.8}$$

Substituting Eq. A.8 into Eq. A.5 and simplifying gives

$$\begin{aligned}\eta &= e''\sin g'' - \tfrac{1}{2}\tfrac{J_3}{J_2}\tfrac{R}{a''}\sin i'',\\ \xi &= e''\cos g''.\end{aligned} \tag{A.9}$$

The expressions for ξ, η mimic the form of Cook's simplified results in Eq. A.4 with the same offset component in η's expression. Moreover, following Davenport (1965), we can write g'' explicitly as

$$\begin{aligned}g'' &= \dot{g}t + g_0'',\\ \dot{g} &= 3n_0\gamma^2\Delta\dot{g},\\ \Delta\dot{g} &= J_2q + \tfrac{1}{8}\gamma^2\left(J_2^2q_{g2} - 5J_4q_{g3}\right),\end{aligned} \tag{A.10}$$

where $q = (5\theta^2 - 1)$, $\theta = \cos i''$, $n_0 = \text{meanmotion} = \sqrt{\frac{\mu}{a''^3}}$, $\gamma = -\frac{1}{2}\frac{R}{a''(1-e''^2)} \approx -\frac{1}{2}\frac{R}{a''}$ (small-eccentricity assumption).

Thus, the final expression for g'' is given by

$$g'' = 3\sqrt{\frac{\mu}{a''^3}}J_2\left(\frac{R}{a''}\right)^2\left(1 - \frac{5}{4}\sin^2 i''\right) + g_0''.$$

Now, under this simplified dynamics, not only do Eq. A.4 in SubSection A.1 and Eq. A.9 have the same form for ξ, η, but also the parameters. The initial condition g_0'' corresponds to the phase ϕ_p; the offset term in the η expression is e_f; the secular eccentricity e'' is exactly the proper eccentricity e_p in both physical meaning and mathematical value.

A.3. Higher-fidelity gravity-harmonics models

While Cook and BL would lead to the same proper elements under equivalent assumptions, it is instructive to uncover and highlight the limitations of the analytical approaches. When eccentricities of $\mathcal{O}(e^2)$ are permitted in the averaged dynamics, Eq. A.3 would show that the eccentricity changes explicitly in the equations. Even for eccentricities $\sim$0.05, the constancy of analytical proper elements, quantified by the range of proper-element oscillations, would change with this increased sophistication. The more complete averaged equations of motion in this case are

$$\begin{aligned}\dot{\eta} &= 3J_2\left(\tfrac{\mu}{a^3}\right)^{1/2}\left(\tfrac{R}{a(1-e^2)}\right)^2\left(1 - \tfrac{5}{4}f\right)\xi,\\ \dot{\xi} &= -3J_2\left(\tfrac{\mu}{a^3}\right)^{1/2}\left(\tfrac{R}{a(1-e^2)}\right)^2\left(1 - \tfrac{5}{4}f\right)\eta\\ &\quad -\tfrac{3}{2}\left(\tfrac{\mu}{a^3}\right)^{1/2}J_3\left(\tfrac{R}{a(1-e^2)}\right)^3\left(1 - \tfrac{5}{4}\sin^2 i\right)\sin i.\end{aligned} \tag{A.12}$$

Taking the same concept of proper and forced elements, but now under the dynamics specified by Eq. A.12, we calculated the analytical proper eccentricity following Cook's formulation for the frozen condition, but employing the vector-difference method from Rosengren et al. (2019a), and the numerical proper eccentricity, applying the Ptolemy method from Wu and Rosengren (2019), detailed in Section 2, for a circumterrestrial space object. Comparing

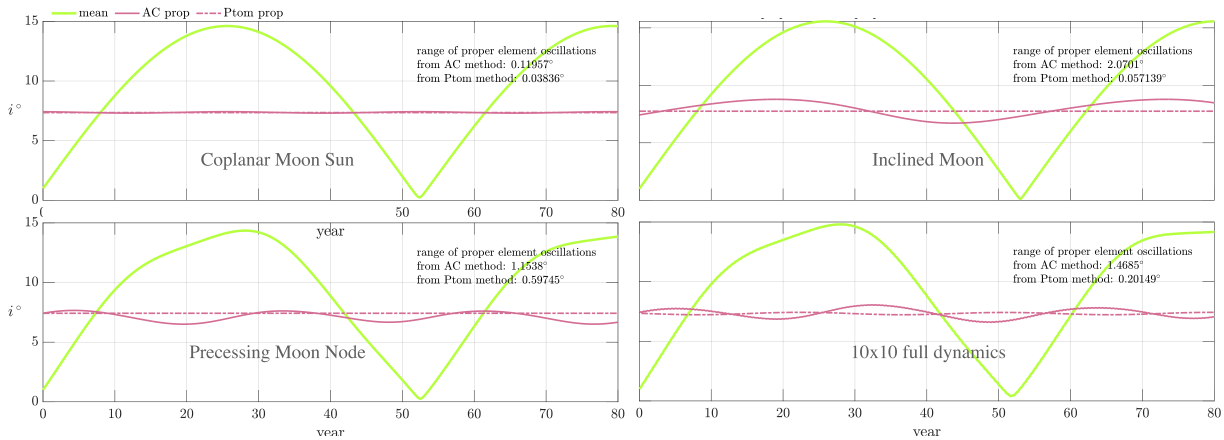

Fig. A.11. Mean and proper inclinations under a hierarchy of dynamical models governing the combined lunisolar and Earth J2 dynamics. The range of proper-element oscillations is shown as an indicator of constancy. The initial mean elements in all cases are $a = 42164.2$ km, $e = 0, i = 1^\circ, \Omega = 100^\circ, \omega = 0^\circ$, and $M = 0^\circ$. The mean-element evolution in the *top panels* is obtained from Eqs. A.13 and A.16, respectively. In the *bottom-left panel*, Eq. A.16 are propagated allowing for the Moon's node to precess. In the *bottom-right panel*, `THALASSA` is used to propagate a full model, including 10×10 Earth harmonics, lunisolar perturbations, atmospheric drag, and SRP dynamics, and the output is numerically converted into mean elements. The analytical AC proper inclinations are obtained from the vector difference method, taking the theoretical frozen inclination of Eq. A.15.

the *top-left panel* of Fig. A.10 to the *top-right panel* shows that the range of proper-element oscillations of the Cook proper eccentricity increases dramatically after employing the more sophisticated dynamics model, but it is still sufficiently small that the near constancy feature of proper eccentricity is unharmed. In addition, both the Cook proper and Ptolemy proper elements yield the same level of range of proper-element oscillations.

We compared three proper elements calculation methods for proper eccentricity under the two different dynamics: simplified J2, J3 dynamics (Eq. A.4) and and full J2, J3 dynamics (Eq. A.12). Beside the aforementioned analytical Cook and numerical Ptolemy methods, we also employed the synthetic approach which is widely accepted as the standard procedure for computing asteroid proper elements in Knežević and Milani (2000, 2002). In Table A.2, comparing the range of proper-element oscillations, as an equivalent indicator for constancy, the Ptolemy method gives a similar constancy yet surpasses the performance of the synthetic approach. Furthermore, when the small eccentricity is expressed explicitly to increase the dynamics model complexity, as discussed before, both the analytical and Ptolemy methods give the same magnitude in ranges of proper-element oscillations, while still outperforming the synthetic method. Interestingly, the range of proper-element oscillations in the synthetic method from the two dynamics models are largely unchanged, mostly because the accuracy represented by this range of proper element oscillations is already "big" so that the model has not had enough difference to affect the value by large.

Table A.2
Range of proper-eccentricity oscillations from multiple models.

	Simplified J2, J3 dynamics	Full J2, J3 dynamics
Analytical	4.3021×10^{-16}	3.5862×10^{-6}
Ptolemy	1.5959×10^{-15}	3.5862×10^{-6}
Synthetic	4.5055×10^{-5}	4.4965×10^{-5}

The additional panels (*middle-right*, *bottom-left*, *bottom-right*) of Fig. A.10 show how the analytical proper elements degrade with additional model complexity. Fig. A.10 (*middle-right*) considers the zonal harmonics up to degree 4, Fig. A.10 (*bottom-left*) considers a 4×4 gravity-field model, and Fig. A.10 (*bottom-right*) includes 10×10 Earth harmonics, lunisolar perturbations, atmospheric drag, and solar radiation pressure dynamics. In these cases, the non-averaged dynamics were propagated using the accurate `THALASSA` Earth-satellite orbit propagation tool (Amato et al., 2019) and a numerical averaging (Izzo et al., 2017) was performed on the osculating dynamics to obtain the mean-element time histories shown therein.

We have shown that while the constancy of proper elements is model-dependent, the concept of proper elements are valid even under increased dynamical fidelity. Proper elements start to deviate from their ideal constant values under more sophisticated models. Despite the divergence from idealized constancy, the concept is still valid for the general case as the oscillations in proper elements, quantified by the absolute difference in their range, is nevertheless still small. Furthermore, we compared the four proper elements calculation methods: analytical Cook, analytical BL, numerical Ptolemy, and numerical synthetic, and showed the difference and similarities in the their results.

A.4. Classical Laplace-plane equilibrium

In previous sections, we focused on models for the evolution of the eccentricity vector and proper eccentricity. In this section, we consider the inclination vector evolution for circular orbits ($e = 0$) perturbed by oblateness and lunisolar third-body perturbations. This scenario corresponds to the circular Laplace equilibrium defined in Allan and Cook (1964), Tremaine et al. (2009), Rosengren et al. (2014).

Tremaine et al. (2009) connected the study of the inclination vector evolution with the seminal work from Laplace. In his study of Jupiter's satellite, Laplace recognized that the combined effects of the Sun and Jupiter's oblateness induced a "free" inclination in the satellite's orbit with respect to Jupiter's equator about a "fixed" equilibrium. The plane of equilibrium solution is called the Laplace plane. In the case of circumterrestrial satellites, Allan and Cook (1964) also defined a perturbation-induced frozen plane under the third-body perturbations, including the Sun and the Moon, and Earth's oblateness J2, which lies between the Earth's equatorial and orbital (ecliptic) planes. Later, Rosengren et al. (2014) adopted the concept of "frozen/forced" in the classical Laplace-plane description, arguing that the secular orbital evolution driven by the combined effects of these perturbations is zero, so those orbits are, *de facto*, frozen.

Since the initial mean eccentricity is 0, the orbit will stay circular on average under this dynamics model, as indicated in Rosengren et al. (2014). So there is only one differential equation for the scaled angular momentum vector, written in terms of the Milankovitch orbital elements. Assuming the Moon lies within the Earth's ecliptic plane, the doubly averaged dynamics for a circular orbit under Earth J2, the Moon, and the Sun, can be written as

$$\dot{\boldsymbol{h}} = -\frac{\omega_2}{h^5}(\hat{\boldsymbol{p}}\cdot\boldsymbol{h})\hat{\boldsymbol{p}}\times\boldsymbol{h} - (\omega_m+\omega_s)(\hat{\boldsymbol{H}}_s\cdot\boldsymbol{h})\hat{\boldsymbol{H}}_s\times\boldsymbol{h}, \quad (A.13)$$

where $\boldsymbol{h} = \boldsymbol{H}/\sqrt{\mu a}$ ($\boldsymbol{H} = \boldsymbol{r}\times\boldsymbol{v}$ is the angular momentum vector), $\hat{\boldsymbol{p}}$ is a unit vector aligned with the maximum axis of inertia of the Earth (i.e. Earth's rotation pole), $\boldsymbol{H}_s$ is a unit vector aligned with the angular momentum vector of the Sun's orbit (i.e., Earth's orbit pole), and

$$\omega_2 = \frac{3nJ_2R^2}{2a^2}, \quad \omega_p = \frac{3\mu_p}{4na_p^3\left(1-e_p^2\right)^{3/2}}, \quad (A.14)$$

where $n = \sqrt{\mu/a^3}$ is satellite's mean motion, J_2 the second-order zonal harmonics, R the mean equatorial radius of the Earth, and μ_p, a_p, e_p are the gravitational parameter, semi-major axis, eccentricity of the perturbers (the Sun or the Moon).

In an inertial frame where the Earth's spin axis $\hat{\boldsymbol{p}}$ is fixed along the z-axis, finding the Laplace plane is equivalent to finding the equilibrium solution to Eq. A.13. By setting the left-hand side of Eq. A.13 equal be $\boldsymbol{0}$, we get the equilibrium condition as

$$\tan 2i_f = \frac{\sin 2\epsilon}{\cos 2\epsilon + \frac{\omega_2}{\omega_m+\omega_s}}, \quad (A.15)$$

where $\epsilon = \hat{\boldsymbol{p}}\cdot\hat{\boldsymbol{H}}_s$ is the obliquity of the ecliptic.

This equilibrium condition yields the frozen inclination for the combined J2 and lunisolar perturbations model, for initially circular orbits. The defining variables in the expression are only parameters related to the dynamical model and semi-major axis, and under the averaged model, the latter is invariant; this is equivalent to the concept of the forced eccentricity for the zonal-harmonics-only model, as the equilibrium condition is also "forced" by the dynamics. We denote the equilibrium inclination defining the Laplace plane as i_f. The proper inclination i_p in this case is defined as the magnitude of the vector difference between the inclination vector, $\mathbf{i}$, projected on a certain plane from the Milankovitch variable $\boldsymbol{h}$ in Eq. A.13 and the forced inclination vector. Non-trivially, we choose a plane defined by inclination i and RAAN Ω such that the inclination vector $\mathbf{i} = (i\sin\Omega, i\cos\Omega)$, and in this case the forced inclination vector would be $\mathbf{i}_f = (0, i_f)$. On this plane, the evolution of inclination vector $\mathbf{i}$ could be decomposed as two vectors: a constant forced inclination vector $\mathbf{i}_f$ and a rotating proper inclination vector $\mathbf{i}_p$.

In Fig. A.11 (*top-left panel*), we applied the analytical method based on vector difference and the AC (Allan-Cook) dynamics formulation and the numerical Ptolemy method to calculate the proper inclination in this classical Laplace-plane dynamics model. The coplanar motion of the Moon and the Sun, both residing on the ecliptic plane, is the only assumption. Proper inclination is quasi-constant, as, from both methods, proper inclination has a much smaller oscillation compared to the mean inclination. And similarly to the idealized case for the eccentricity shown in Fig. A.10 (*top-left panel*), the proper inclinations from Ptolemy and the analytical method have comparable oscillations represented by their ranges of proper-element oscillations.

A.5. Laplace-plane dynamics model with inclined and precessing Moon

A more realistic model would consider the Moon's ecliptic inclination such that its orbit pole is not aligned with that of the Sun (i.e., $\hat{\boldsymbol{H}}_m \neq \hat{\boldsymbol{H}}_s$). The doubly averaged dynamics for this case can be expressed as

$$\dot{\boldsymbol{h}} = -\frac{\omega_2}{h^5}(\hat{\boldsymbol{p}}\cdot\boldsymbol{h})\hat{\boldsymbol{p}}\times\boldsymbol{h} + \omega_s(\hat{\boldsymbol{H}}_s\cdot\boldsymbol{h})\hat{\boldsymbol{H}}_s\times\boldsymbol{h} + \omega_m(\hat{\boldsymbol{H}}_m\cdot\boldsymbol{h})\hat{\boldsymbol{H}}_m\times\boldsymbol{h}. \quad (A.16)$$

The motion of the orbit pole of the satellite in this case is a combination of simultaneous precession about these three different axes, one of which, the pole of the Moon's orbit, regresses around the pole of the ecliptic with a period of 18.61 years. Even when ignoring the Moon's nodal motion and assuming that $\hat{\boldsymbol{H}}_m$ is fixed, there is no longer a corresponding equilibrium or fixed inclination.

The *top-right* and *bottom-left panels* of Fig. A.11 shows the mean-element evolutions obtained from simulating Eq. A.16 fixed-inclined and precessing lunar orbit, respectively.

While the quasi-constancy of the analytical AC proper inclination changes dramatically with the Moon's inclination and nodal precession considered, the numerical Ptolemy proper inclination stays almost the same. We have shown a similar performance in proper eccentricity in Fig. A.10 (*top-right panel*) that the numerical proper elements from the Ptolemy method is less sensitive to dynamics model sophistication than for the analytical method. Fig. A.11 considers a full dynamical model propagated using THALASSA. We note that the range of proper-element oscillations from the numerical proper inclination is of comparable magnitude as proper inclination from the idealized dynamics. While proper inclination's quasi-constancy is most obvious in the simplified model, we have shown that, with a suitable method, even at a more sophisticated level, this property of proper inclination could be conserved.

References

Adams, R.P., MacKay, D.J.C., 2007. Bayesian online changepoint detection. arXiv:0710.3742.

Al-Sharadqah, A., Chernov, N., 2009. Error analysis for circle fitting algorithms. arXiv:0907.0421.

Alfriend, K.T., Vadali, S.R., Gurfil, P., How, J.P., Breger, L.S., 2009. Spacecraft Formation Flying: Dynamics, Control and Navigation. Butterworth-Heinemann, Oxford.

Allan, R.R., Cook, G.E., 1964. The long-period motion of the plane of a distant circular orbit. Proc. Roy. Soc. A 280, 97–109.

Amato, D., Bombardelli, C., Baú, G., Morand, V., Rosengren, A.J., 2019. Non-averaged regularized formulations as an alternative to semi-analytical orbit propagation methods. Celestial Mech. Dynam. Astron. 131 (21), 38.

Bottke Jr., W.F., Vokrouhlický, D., Rubincam, D.P., Nesvorný, D., 2006. The Yarkovsky and YORP effects: Implications for asteroid dynamics. Annu. Rev. Earth Planet. Sci. 34, 157–191.

Breakwell, J.V., Vagners, J., 1970. On error bounds and initialization in satellite orbit theories. Celestial Mech. 2, 253–264.

Brouwer, D., 1951. Secular variations of the orbital elements of minor planets. Astron. J. 56, 9–32.

Brouwer, D., 1959. Solution of the problem of artificial satellite theory without drag. Astron. J. 64, 378–397.

Byers, M., Boley, A., 2023. Who Owns Outer Space? International Law, Astrophysics, and the Sustainable Development of Space. Cambridge University Press, Cambridge.

Cain, B.J., 1962. Determination of mean elements for Brouwer's satellite theory. Astron. J. 67, 391–392.

Celletti, A., Pucacco, G., Vartolomei, T., 2021. Reconnecting groups of space debris to their parent body through proper elements. Nature 11, 22676.

Celletti, A., Pucacco, G., Vartolomei, T., 2022. Proper elements for space debris. Celestial Mech. Dyn. Astron. 134, 11.

Chao, C.C., Hoots, F., 2018. Applied Orbit Perturbation and Maintenances, 2nd ed. Aerospace Press, El Segundo, CA.

Coffey, S.L., Deprit, A., Deprit, E., 1994. Frozen orbits for satellites close to an Earth-like planet. Celestial Mech. Dynam. Astron. 59, 37–72.

Cook, G.E., 1966. Perturbations of near-circular orbits by the Earth's gravitational potential. Planet. Space Sci. 14, 433–444.

Davenport, P.B., 1965. Modification of Brouwer's solution for artificial satellites to include small eccentricities and inclinations. Technical Report X-543 -65-23. NASA Goddard Space Flight Center.

Escribano, G., Sanjurjo-Rivo, M., Siminski, J., Pastor, A., Escobar, D., 2022. Automatic maneuver detection and tracking of space objects in optical survey scenarios based on stochastic hybrid systems formulation. Adv. Space Res. 69, 3460.

Gachet, F., Celletti, A., Pucacco, G., Efthymiopoulos, C., 2017. Geostationary secular dynamics revisited: application to high area-to-mass ratio objects. Celestial Mech. Dynam. Astron. 128, 149–181.

Gander, W., Golub, G.H., Strebel, R., 1994. Least-squares fitting of circles and ellipses. BIT Num. Mathe. 34, 558–578.

Giacaglia, G.E.O., 1974. Lunar perturbations of artificial satellites of the Earth. Celestial Mech. 9, 239–267.

Hirayama, K., 1918. Groups of asteroids probably of common origin. Astron. J. 31, 185–188.

Izzo, P., Dell'Elce, L., Gurfil, P., Rosengren, A.J., 2017. Nonsingular vectorial reformulation of the short-period corrections in Kozai's oblateness solution. Celestial Mech. Dynam. Astron. 134, 12.

Jankovic, M., Kirchner, F., 2018. Taxonomy of LEO space debris population for ADR capture methods selection. In: Vasile, M., Minisci, E., Summerer, L., McGinty, P. (Eds.), Stardust Final Conference: Advances in Asteroids and Space Debris Engineering and Science. Springer, Cham, pp. 129–144.

Kelecy, T., Hall, D., Hamada, K., Stocker, D., 2007. Satellite maneuver detection using two-line element (TLE) data. In: Proceedings of the Advanced Maui Optical and Space Surveillance Technologies Conference.

Knežević, Z., Lemaître, A., Milani, A., 2002. The determination of asteroid proper elements. In: Bottke, W., Jr., Cellino, A., Paolicchi, P., Binzel, R.P. (Eds.), Asteroids III. University of Arizona Press, Tucson, pp. 603–612.

Knežević, Z., Milani, A., 1998. Orbit maintenance of a lunar polar orbiter. Planet. Space Sci. 46, 1605–1611.

Knežević, Z., Milani, A., 2000. Synthetic proper elements for outer main belt asteroids. Celestial Mech. Dynam. Astron. 78, 17–46.

Ko, H., Scheeres, D., 2015. Orbit determination and maneuver detection using event representation with thrust-fourier-coefficients. In: Proceedings of the Advanced Maui Optical and Space Surveillance Technologies Conference (AMOS).

Lara, M., 2021. Hamiltonian Perturbation Solutions for Spacecraft Orbit Prediction: The Method of Lie Transforms. De Gruyter, Berlin/Boston.

Lemmens, S., Krag, H., 2014a. Maneuver detection method based on probability distribution fitting of the prediction error. J. Spacecraft Rock. 56 (4), 7.

Lemmens, S., Krag, H., 2014b. Two-line-elements-based maneuver detection methods for satellites in low earth orbit. J. Guidance Control Dynam. 37, 860.

Li, T., Li, K., Chen, L., 2018. New manoeuvre detection method based on historical orbital data for low-earth orbit satellites. Adv. Space Res. 62, 554.

Lyddane, R.H., 1963. Small eccentricities or inclinations in the Brouwer theory of the artificial satellite. Astron. J. 68, 555–558.

Mellish, R., Frueh, C., 2021. An automated taxonomy for human-made objects in Geosynchronous orbits. J. Astronaut. Sci. 68, 480–502.

Migliorini, F., Michel, P., Morbidelli, A., Nesvorný, D., Zappalà, V., 1998. Origin of multikilometer Earth- and Mars-crossing asteroids: A quantitative simulation. Science 281, 2022–2024.

Milani, A., Cellino, A., Knežević, Z., Novaković, B., Spoto, F., Paolicchi, P., 2014. Asteroid families classification: Exploiting very large data sets. Icarus 239, 46.

Milani, A., Knežević, Z., 1994. Asteroid proper elements: The big picture. In: Asteroids, Comets, Meteors 1993: Proceedings of the 160th Symposium of the International Astronomical Union.

Morbidelli, A., 2002. Modern Celestial Mechanics: Aspects of Solar System Dynamics. Taylor & Francis, London.

Murray, C.D., Dermott, S.F., 1999. Solar System Dynamics. Cambridge University Press, Cambridge.

Nesvorný, D., Brož, M., Carruba, V., 2015. Identification and dynamical properties of asteroid families. In: Michel, P., DeMeo, F.E., Bottke, W.F. (Eds.), Asteroids IV. University of Arizona Press, Tucson, pp. 297–321.

Novaković, B., Vokrouhlický, D., Spoto, F., Nesvorný, D., 2022. Asteroid families: properties, recent advances, and future opportunities. Celestial Mech. Dynam. Astron. 134, 34.

Pastor, A., Escribano, G., Sanjurjo-Rivo, M., Escobar, D., 2022. Satellite maneuver detection and estimation with optical survey observations. J. Astronaut. Sci. 69, 879.

Pirovano, L., Armellin, R., 2022. Detection and estimation of spacecraft maneuvers for catalog maintenance. arXiv:2210.14350.

Porcelli, L., Pastor, A., Cano, A., Escribano, G., Sanjurjo-Rivo, M., Escobar, D., Lizia, P.D., 2022. Satellite maneuver detection and estimation with radar survey observations. Acta Astronaut. 201, 274.

Rein, H., Spiegel, D.S., 2015. IAS15: a fast, adaptive, high-order integrator for gravitational dynamics, accurate to machine precision over a billion orbits. Mon. Not. R. Astron. Soc. 446, 1424–1437.

Rosengren, A., Amato, D., Bombardelli, C., Jah, M., 2019a. Resident space object proper orbital elements. In: Proceedings of the AAS/AIAA Space Flight Mechanics Conference.

Rosengren, A.J., Scheeres, D.J., McMahon, J.W., 2014. The classical Laplace plane as a stable disposal orbit for geostationary satellites. Adv. Space Res. 53, 1219–1228.

Rosengren, A.J., Skoulidou, D.K., Tsiganis, K., Voyatzis, G., 2019b. Dynamical cartography of Earth satellite orbits. Adv. Space Res. 63, 443–460.

Schaub, H., Junkins, J.L., 2018. Analytical Mechanics of Space Systems, 4th ed. American Institute of Aeronautics and Astronautics, Reston.

Tremaine, S., Touma, J., Namouni, F., 2009. Satellite dynamics on the Laplace surface. Astron. J. 137, 3706–3717.

Vallado, D.A., 2022. Fundamentals of Astrodynamics and Applications, 5th ed. Microcosm, Hawthorne, CA.

Walter, U., 2018. Astronautics: The Physics of Space Flight, 3rd ed. Springer, Cham.

Wu, D., 2022. New Dynamical Connections Between Circumterrestrial Space Objects and Small Solar System Bodies. University of California San Diego, Ph.D. thesis.

Wu, D., Rosengren, A., 2019. Analysis of proper elements for resident space objects. In: 70th International Astronautical Congress.

Zappalà, V., Cellino, A., Farinella, P., Knežević, Z., 1990. Asteroid families. I. identification by hierarchical clustering and reliability assessment. Astron. J. 100.

Zucchelli, E., McLaughlin, Z., Jones, B., 2020. Tracking maneuvering targets with multi-fidelity interacting multiple model filters. In: Proceedings of the Advanced Maui Optical and Space Surveillance Technologies Conference (AMOS).